The brittle-to-ductile transition in cold-rolled tungsten sheets: Contributions of grain and subgrain boundaries to the enhanced ductility after pre-deformation

Carsten Bonnekoh[a,*,5], Philipp Lied[a,1], Stefan Zaefferer[b], Ute Jäntsch[a], Andreas Hoffmann[c,2], Jens Reiser[a,3], Michael Rieth[a,4]

[a] *Karlsruhe Institute of Technology, Institute for Applied Materials - Applied Materials Physics, 76344 Eggenstein-Leopoldshafen, Germany*
[b] *Max-Planck-Institut für Eisenforschung GmbH, Department Microstructure Physics and Alloy Design, 40237 Düsseldorf, Germany*
[c] *Plansee SE, 6600 Reutte, Austria*

ARTICLE INFO

ABSTRACT

One of the key demands on tungsten (W) as designated plasma-facing material (PFM) is the capability to fulfill a structural function. Since W has refused ductilization strategies by alloying alone, the production of W materials with enhanced ductility has come into focus considering tailored microstructures. This work addresses the rolling-induced microstructural modifications of warm- and cold-deformed W sheets and is supplemented by a comprehensive fracture mechanical study as a fundament for correlations between the spatial distribution of boundaries and brittle-to-ductile transition (BDT) temperature. Here we show that an extended Hall–Petch-like relationship is well suited to describe the rolling-induced reduction in BDT temperature and moreover has the potential to reflect the anisotropic nature of the transition temperature in severely rolled W sheets. Using the data of warm- and cold-rolled W sheets and also of strongly recovered W, best description of the BDT temperature was achieved by using as microstructural variables (i) the mean spacing between boundaries which intersect with the crack front and (ii) the mean boundary spacing along the normal of the crack plane. Taking into account the similarity to recent simulative-derived relationships, our findings support the theory suggesting the stimulated dislocation nucleation at boundaries as the decisive factor for more effective shielding of the crack tip in UFG materials and, in consequence, significantly reduced BDT temperatures. Besides, this work gives strong indications that the reduction of the BDT temperature in UFG W is not related to coincidence site lattice (CSL) boundaries.

1. Introduction

During the operation of fusion reactors, plasma-facing materials (PFMs) are exposed to high fluences of neutrons and have to withstand highest thermal loads. Low rates of sputtering erosion favor high-Z materials as divertor PFM [1]. Among these materials, tungsten (W) is the front-runner candidate at the present moment [2]. However, its high brittle-to-ductile transition (BDT) temperature and, as a result,

brittle material behavior at room temperature, challenges the application of W [3]. To give numbers: W with a recrystallized microstructure exhibits usually BDT temperatures, which are around 650 K [4] using notched specimens under quasi-static loading and 1000 K [5] in Charpy impact experiments. Even worse than the recrystallized conditions behaves as-sintered W [6], having BDT temperatures in the range 900 K-1100 K [7–9] and in the region around 1200 K for dynamic loading rates (all temperatures are related to notched specimens). Worked W

---

grades that are commercially available exhibit usually slightly lower BDT temperatures, which depend de facto on the production history, e.g. [5,10–13]. Since W components are also foreseen to fulfill safety-relevant structural functions [14] and moreover as base material for pressurized parts in the He-cooled divertor concept [15,16], there is demand in W materials which ensure fail-safe operation and allow an industrial-scale production [17].

Research has been strongly focusing on improving the crack resistance of W at lower temperatures utilizing extrinsic and intrinsic toughening strategies [18], i.e. W fiber-reinforced W [19] or composite W materials [20] or achieving this goal by ductilization. The latter (intrinsic) strategy implies in the first place a reduction of the BDT temperature concentrating on the processes taking place in front of the crack tip. Since the chemical composition and microstructure influence the transition temperature [21], both approaches might help to realize room-temperature ductility. In this work, we use the term room-temperature ductility to describe a material condition that exhibits substantial amounts of stable crack propagation at room temperature as a result of a BDT temperature below room temperature. However, W has manifested its refractarius nature by refusing substantial progress in improving ductility by using materials with ultra-low impurity concentration [22] and by alloying approaches as well [23]. Alloys composed by elements with full solubility (V, Nb, Mo, and Ta) behave in first approximation as bad as their technical pure counterparts or exhibit even higher BDT temperatures [24]. For more details concerning these alloys we refer the reader to the regarding works [25–27] for W-V alloys, [28] for approaches using Nb, [29] for the W-Mo system, and [9,25,27,28,30], which are dealing with W-Ta alloys. Own results on the Charpy impact properties of W-Mo will be the subject of future publications.

A unique feature of metals with high lattice friction for dislocation glide is the effect of solid solution softening (SSS), reducing the critical resolved shear stress and causing a ductilization by small additions of foreign elements [31]. Among the elements with relevant but limited solubility (here: some at.-% in equilibrium at low temperatures) in W, which are to our best knowledge [32–36] Al, Ti, Tc, Ru, Rh, Re, and Os; a clear solid solution softening effect at room temperature has been experimentally found for the Group VII-B elements Tc, Re [37–41] and in Group VIII-A adding Ru, Os [37,41,42]. Reduced hardness has been also observed after micro-alloying of VIII-B element Ir [38,41,43] and VIII-C Pt [41,43]. This demonstrates the importance of the electron configuration of the valence shell for solid solution softening, which has been addressed in recent DFT calculations [44,139]. Rare deposits and high costs of these elements have prevented widespread use of W alloys containing solid solution softening elements. Furthermore, the SSS effect is temperature-dependent and reverses for elevated temperatures, which is labeled as solid softening-to-hardening transition [140]. For W-Re alloys, the shift of the Re concentration that is related to the hardness minimum (reducing with increasing material temperature) has been comprehensively studied [141,39]. For other alloying elements, little information is currently available for temperatures that differ from room temperature [40,142]. To our best knowledge solely W-Tc and W-Re alloys have been proven to exhibit also significantly reduced BDT temperatures [8,37,41,45,46]. The fact that Tc needs be extracted from spent nuclear fuel, and the fast radioactive decay of some Tc isotopes [47], makes the use of W-Tc alloys seriously impractical. It is furthermore believed that also small Ir and Os additions are beneficial for achieving lower BDT temperatures, however, experimental data about these alloys are sparsely [41]. Up to the present days, solely the W-Re system has gained commercial importance [48] in the background of improving the mechanical behavior of W. Alloys with Re contents close to the solubility limit show significantly improved ductility in comparison to pure W [49]. Even room-temperature ductility has been reported for worked material conditions using notched specimens [50]. After 1 h annealing at about 1900 K [28] and beyond [51] room-temperature ductility was retained in bending

experiments using unnotched specimens, which make Re to the most promising alloying element for the ducilization of W.

Plasma facing materials are exposed to high fluences of fast and thermal neutrons during reactor operation [52], causing accumulative modifications in physical and engineering properties, furthermore the generation of transmutation products and volumetric swelling [53–55], whereby the single amounts are strongly influenced by the neutron spectra [56]. Irradiation hardened W [57]. exhibits BDT temperatures that are significantly higher than the high values observed for W in general [58,59]. Post-irradiation investigations have turned out that under neutron bombardment W-Re alloys tend to form significant amounts of needle-shaped intermetallic phase precipitations inconsistent with the phase diagram [60]. The higher the Re content, the more precipitations form at a given dose and spectrum [52], deteriorating ductility clearly below the level of pure W that was exposed to a similar irradiation conditions [61]. On the other hand, Re addition is an effective strategy to suppress void formation [62], which is the most essential irradiation defect in pure W. To meet all the requirements for a future PFM, clever-composed W-Re alloys are needed, cf. scheme developed by Fukuda et al. [63].

There is a switchover in major structural defect from loop damage to embrittlement caused by needle-shaped precipitations, which takes place around 10% Re [52]. Considering the predicted breeding of Re during component lifetime [64], the best compromise in alloy design has been suggested to be between 1 and 3 wt-% Re concentration [52]. Consequently, room-temperature ductility of W cannot be achieved by applying an alloying strategy alone. This has been confirmed also by recent Charpy results on rolled and stress relieved W-3Re [65] and W-3Re-K [66] alloys, exhibiting a slightly reduced transition temperature compared to that predicted by a grain size-adjusted trend based on experimental results for pure W. This indicates that the reduced BDT temperature of W-3Re alloys is less an effect of solid solution softening, rather than the consequence of a reduced grain size during a similar production route.

Significant improvements in terms of a reduced BDT temperature have been achieved by generating ultrafine-grained (UFG) microstructures by an industrial-scale rolling process [5,67–69]. Stable crack propagation far below room-temperature makes cold-rolled W to the ones with the lowest BDT temperatures [7,70] among all W materials without substantial Re additions. These improvements assign microstructure engineering as the decisive role for developing concepts for future PMFs. Since we have shown in earlier works [4,71] that the rate-limiting process of crack tip plasticity in UFG W is still the glide of the ½⟨111⟩ screw segments, the contribution of lattice defects in UFG microstructures to room-temperature ductility has come to focus of interest. With this paper, we attempt to answer the following open questions:

(1) Which rolling-induced modifications in boundary properties and dislocation structure can be observed after severe rolling?
(2) What is the impact of grain and subgrain boundaries concerning the reduced BDT temperatures of severely rolled W sheets?
(3) Is room-temperature ductility after cold rolling the consequence of a raised generation of coincidence site lattice (CSL) boundaries during pre-deformation at these low temperatures?

This paper is organized as follows: First, the impact of pre-deformation on the BDT temperature is assessed. Then, we show the results of a comprehensive microstructural characterization and make attempts to link the evolution of the microstructure with the change in BDT based on recent simulation-derived relationships.

2. Material and methods

The impact of plastic deformation on microstructure and transition temperature was studied using W sheets which were rolled to different

Table 1

Thickness reduction by rolling and preheating temperatures. The materials' labeling represents the logarithmic strain conducted by warm and cold rolling (ε_{Log}) extended by the rolling temperatures (warm rolling: WR and cold rolling: CR). The relative reductions (Δt) in percent are listed in comparison to the hot-rolled (HR) state. The preheating temperatures ($T_{\text{Preheating}}$) selected for warm and cold rolling are expressed as homologous temperatures, i.e. as a fraction of the melting temperature (T_{Melt}), which is about 3700 K for pure W [24]. Furthermore, the average surface roughness (Ra) of the sheets is given, cf. Ref. [73].

Material	$T_{\text{Preheating}}$/K	ε_{Log}/-	Δt/%	t_{Sheet}/mm	Ra/μm
1.7WR	$< 0.4 \times T_{\text{Melt}}$	HR + 1.7	82	1.091 ± 0.007	2.08 ± 0.25
2.5WR	$< 0.4 \times T_{\text{Melt}}$	1.7 + 0.8	91	0.521 ± 0.004	1.56 ± 0.31
2.9WR	$< 0.4 \times T_{\text{Melt}}$	2.5 + 0.4	94	0.343 ± 0.005	1.40 ± 0.64
3.3WR	$< 0.4 \times T_{\text{Melt}}$	2.9 + 0.4	96	0.221 ± 0.010	1.02 ± 0.11
4.1CR	$< 0.2 \times T_{\text{Melt}}$	3.3 + 0.8	98	0.106 ± 0.004	0.29 ± 0.08

strains. By utilization of a single hot-rolled plate as starting material and sampling the sheets after specific rolling steps, variations in chemical composition between these sheets were avoided.

2.1. Materials: Warm and cold rolling

Sheet production was realized in cooperation with Plansee SE, Austria by applying a proprietary rolling method. The sheets 1.7WR, 2.5WR, 2.9WR, and 3.3WR, were produced in sequence conducting warm rolling (WR), whereby the label number indicates the logarithmic strain conducted by rolling after the last pass of hot-deformation. The material denoted as 4.1CR was produced by applying to the material 3.3WR an additional thickness reduction of 0.8 logarithmic strain by cold rolling (CR). Warm and cold rolling was carried out in a strictly unidirectional manner. Rolling parameters are summarized in Table 1. The distinctions in hot-, warm- and cold-worked materials are based on the suggestions by Trefilov et al. [72] for bcc refractory metals. All materials remained in as-rolled condition without any further heat treatment.

2.2. Fracture mechanical testing: BDT temperature

In this work, single edge notched tensile SE(T) specimens equipped with L-T crack system [74] were tested, cf. Fig. 1 for the specimen geometry, specimen alignment with respect to the rolling direction and used sample fixture. Except pickling, no further surface treatment was subjected to the sheets. Consequently, surface quality and thickness of the specimens used for fracture mechanical testing are predetermined by the sheet properties, cf. Table 1. The outer specimen geometry and notch were machined using electro-discharge machining (EDM) leading to a notch with a radius of about 0.07 mm at its tip. As it is accepted practice for W, an additional fatigue pre-crack was not inserted [59,75,76]. As a result, crack propagation starts at the tip of the EDM notch, which is decorated with multiple short cracks, cf. Ref. [7] for micrographs of the crack tip.

A universal mechanical testing machine (ZwickRoell 1474, Germany) equipped with an environmental chamber (Instron SFL 3119–400, USA) was used for all fracture toughness tests, covering test temperatures between 120 K and 473 K. Loading of the SE(T) specimens was applied in displacement-controlled mode (constant crosshead speed) leading to a mode I type of crack opening [77]. All the tests were run in air. During the test campaigns, three nominal loading rates were applied: 0.01, 1.0, and 100 MPa m$^{0.5}$ s^{-1}. The actual loading-rates are listed in Table 2. After each experiment, the critical stress intensity factor (K_Q) was determined following the procedure given in ASTM E399 [74]. As a result of the test campaigns, trends showing the evolution of the critical stress intensity factor against the test temperature were generated. On that basis, the respective BDT temperatures were determined cf. Table 2.
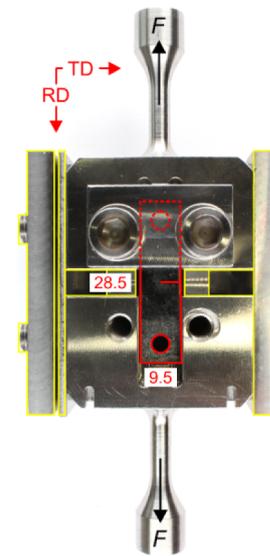

Fig. 1. Specimen, specimen fixture, and assembly device. Specimen geometry and outer specimen dimensions are highlighted in red. The thickness of the specimens varies and is equal to the thickness of the respective sheet. Furthermore, the alignment of the rolling direction (RD) and transverse direction (TD) with respect to the notch position is provided. Components of the assembly device are bordered in yellow. A detailed sketch of the experimental setup is given in an earlier publication [7]. (For interpretation of the references to color in this figure legend, the reader is referred to the web version of this article.)

At this point, we like to emphasize that the determined fracture toughness values are very likely non-conservative, due to a significant material fraction in plane stress condition (thin sheets). The absence of a fatigue pre-crack is assumed to increase the measured critical stress intensity factor additionally [75]. However, our experiments do not have the objective to determine values of the plane strain fracture toughness (K_{Ic}), which is a material property. Instead, trends for the determination of BDT temperatures were recorded.

2.3. Electron backscatter diffraction: boundary-related properties

Specimens for microstructural investigations were cut from the sheets by EDM and embedded in a hard compound as a mechanically clamped stack of specimens. The surface layer affected by EDM was removed by careful grinding. Due to mechanical and subsequent electrochemical polishing, we ensure smooth sample surfaces (surface roughness Rt below 100 nm) and a minimum of preparation-induced defects. As etching agent we used an aqueous solution containing demineralized H_2O and 0.66 wt-% NaOH, which is a diluted ASTM electrolyte VII-7 [78]. A voltage of 10 V for a net time of 180 s was applied, activated in pulses as a sequence of 5 s current and 10 s time-out.

Electron backscatter diffraction (EBSD) maps were acquired using a high-resolution field emission SEM MERLIN (Carl Zeiss Microscopy, Germany) equipped with a Hikari XP (EDAX, USA) EBSD detector. An acceleration voltage of 15 kV, probe current of 20 nA and a step size of 40 nm was selected for all mappings. The EBSD camera was operated applying a 4x4 binning. Cross-sections defined by RD and ND [74] were scanned. Four maps, with an area of 35 μm by 45 μm each, were recorded along the centerline of every sheet. The same procedure was carried out for the cross-sections defined by TD and ND. More than 2000 grains are covered per material and cross-section. At least 96% of the pixels per dataset had a confidence index (CI) of 0.1 or above before post-processing. Pixels with a CI below 0.1 were eliminated during post-processing utilizing TSL OIM Analysis v8. Beyond that, only grain CI standardization (CIS) was applied as cleanup routine, leaving the measured orientation of all the points unchanged.

Table 2

BDT temperatures and related loading rates. The BDT temperatures determined using a LT crack system ($T_{\text{BDT|LT}}$) are given as a rate-dependent property for the three nominal loading rates applied in this study. The actual loading rates are listed as mean values calculated based on all semi-ductile and ductile specimens in the respective test campaign, tested at the BDT temperature and at directly neighbored test temperatures.

Material	$T_{\text{BDT|LT}}^{0.01}$/K	$\mathbf{d}K/\mathbf{d}t^{0.01}$/MPa m$^{0.5}$ s^{-1}	$T_{\text{BDT|LT}}^{1.0}$/K	$\mathbf{d}K/\mathbf{d}t^{1.0}$/MPa m$^{0.5}$ s^{-1}	$T_{\text{BDT|LT}}^{100}$/K	$\mathbf{d}K/\mathbf{d}t^{100}$/MPa m$^{0.5}$ s^{-1}
1.7WR	385	0.0090 ± 0.0004	398	1.00 ± 0.06	473	101.2 ± 14.5
2.5WR	298	0.0213 ± 0.0019	348	1.08 ± 0.04	398	120.2 ± 13.3
2.9WR	310	0.0121 ± 0.0010	323	1.03 ± 0.06	398	120.8 ± 4.4
3.3WR	283	0.0072 ± 0.0009	323	1.18 ± 0.04	360	78.8 ± 11.6
4.1CR	173	0.0172 ± 0.0004	208	1.08 ± 0.11	236	116.5 ± 12.9

Following Hansen et al. [79], we define high-angle boundaries (HABs) as boundaries between points with a lattice disorientation angle above 15°, and low-angle boundaries (LABs) with lattice disorientation angles between 2° and 15°.

2.4. Electron channeling contrast imaging: Dislocation structure

Basic specimen preparation for ECCI was identical to the procedure as described for EBSD. After electrochemical polishing, focus ion beam (FIB) milling, using a FIB-SEM AURIGA (Carl Zeiss Microscopy, Germany) with a gallium probe, was applied to mark specific areas on the sample surfaces applying a probe current of 1 nA and 30 kV as acceleration voltage for the Ga ions. After that, the specimens were electrochemically polished again for six pulses (see above) to remove the surface layer containing ion beam damage. Finally, mechanical polishing with colloidal silica for around 120 s was carried out to remove thin oxide layers caused by electrochemical polishing.

For best beam convergence the SEM MERLIN was operated with an acceleration voltage of 30 kV and a probe current of 2 nA. A retractable 4-quadrant backscattered electron detector (BSD) was used and the sample was positioned at a working distance of 6 mm. We inverted the signal of the BSD on all four sectors to obtain an image contrast, which is well-known from TEM micrographs acquired in bright-field conditions. The orientation of the investigated grains was measured by EBSD scans of the region of interest. Therefore, the sample was tilted to 70° under retaining the selected region of interest by using the applied FIB markings on the sample surfaces as an orientation. Information from the micrographs and orientation information was coupled with the software T.O.C.A. v2.3 [80], after initial calibration of the orientation relationship between BSED and EBSD detector.

3. Results

Here, we elucidate the rolling-induced evolution in BDT temperature and lattice defects of W sheets. These results are the fundament for the later empirical study on the influence of boundaries on the transition temperature in W sheets.

3.1. Shift in BDT temperature by pre-deformation

In the following section we address the impact of pre-deformation on the BDT temperature of W sheets. Our results reveal a reduction of BDT temperature with increasing plastic strain conducted by rolling. Cold rolling appears to be most effective.

Campaigns of fracture toughness tests were carried out to acquire trends of the critical stress intensity factor (K_{Q}) against the test temperature (T). For each sheet three trends were recorded, which are related to the nominal loading rates 0.01, 1.0, and 100 MPa m$^{0.5}$ s^{-1}. These trends are shown in Fig. 2. Diagrams for the same material condition but different loading rates are aligned horizontally, while diagrams for different materials are aligned vertically (See notation in the top left corners with material and loading rate). Following Schwalbe et al. [81], we categorize the material behavior in the following groups: (i) brittle behavior (filled symbols): fracture unstable

and linear force–displacement behavior, (ii) semi-ductile behavior (crossed symbols): fracture unstable and curve non-linear (test record intersects at least with 95%-tangent [77], representing stable crack propagation across approximately 2% of the ligament width), and (iii) ductile behavior (open symbols): fracture stable and non-linear curve in force against displacement plot. Based on this classification, we define the BDT temperature (for the given material and the respective loading rate) as the lowest test temperature in the respective test campaign exhibiting solely ductile or semi-ductile material behavior, but without any specimen which has failed in a brittle manner.

Studying the evolution of material behavior with increasing logarithmic strain (from the top row downwards in Fig. 2), a clear trend towards lower BDT temperatures can be observed. This statement is general, i.e. independent of the applied loading rate and therefore we mainly focus on the trends acquired at the intermediate loading rate 1 MPa m$^{0.5}$ s^{-1} (center column) hereinafter. At the intermediate loading rate, the less deformed material condition (material 1.7WR) exhibits a BDT temperature of 385 K. This is above the remaining warm-rolled materials (2.5WR, 2.9WR, and 3.3WR), with BDT temperatures of 348 K, 323 K, and once again 323 K. Thus, the decrease in BDT temperature achieved by an additional warm deformation (a logarithmic strain of 1.6 in maximum) is limited to reductions in transition temperature of − 50 K and − 75 K, respectively. A more substantial reduction of the BDT temperature can be seen after further cold rolling. With 208 K, the transition temperature of the cold-rolled material 4.1CR shows clearly the lowest value which represents a further reduction of − 115 K with regard to material 3.3WR. Therefore, among the produced set of five sheets, material 4.1CR is the only one that shows stable crack propagation at room-temperature. With a BDT temperature of 236 K, room-temperature ductility is even maintained at the accelerated loading rate. We want to highlight that the various thicknesses of the specimens (as a consequence of the different strains conducted by rolling) can be neglected in the discussion of the BDT temperature. Our results have demonstrated (to be published) that in the thickness region studied in this work the BDT temperature is not affected by the specimen thickness or only slightly, so that this effect vanishes in the experimental scatter.

3.2. Rolling-induced deformation structure

Here, we describe the microstructural evolution as a result of increasing strain conducted by rolling. Grain size reduction and an evolution towards a HAB dominated microstructure are quantified. We also observe changes in the dislocation structure between warm-rolled and cold-rolled W.

In Fig. 3 a part of the acquired EBSD data is illustrated, giving a first idea of the modifications in microstructure that took place during each rolling step. Strain conducted by rolling is increasing from top to bottom. The magnification of the maps increases from left to right column, starting with overview maps, which provide representative impressions of respective microstructures at the centerline of the respective sheets. At the center column, sections of the respective overview maps are shown at an intermediate magnification, revealing more details of single microstructural features like HABs and LABs, which are
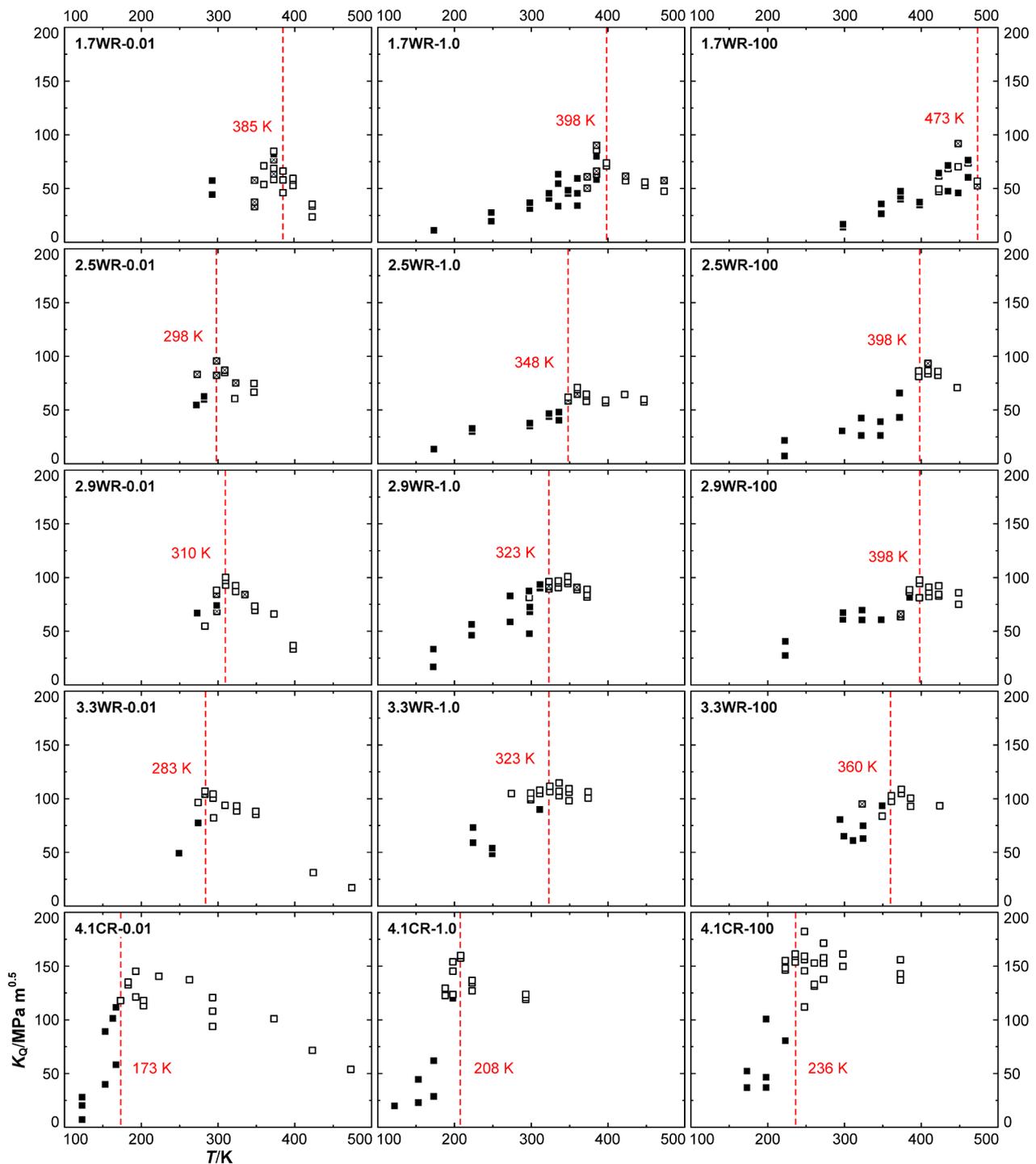
Fig. 2. Impact of rolling on the BDT temperature. Trends of the critical stress intensity factor (K_Q) are plotted against the test temperature (T). Each subplot displays the results of one material condition tested at a constant loading rate. Each row of subplots shows the test campaigns for one of the five tested material conditions with different logarithmic strain (1.7WR to 4.1CR), as noted in the top left corner. Each column of subplots separates the test campaigns by the applied loading rates (dK/dt) of 0.01 MPa m$^{0.5}$ s^{-1}; 1.0 MPa m$^{0.5}$ s^{-1} and 100 MPa m$^{0.5}$ s^{-1}, as indicated in the top left corner as well. Additionally, the filling of the symbols reflects the material behavior observed in the respective single experiment. Filled symbols represent brittle behavior, crossed symbols semi-brittle and open symbols indicate ductile material behavior, respectively (for explanation see text). The vertical lines (red dashed) highlight the deduced BDT temperatures. (For interpretation of the references to color in this figure legend, the reader is referred to the web version of this article.)

highlighted in black and white, respectively. The regions covered by these sections are enclosed by black-white frames. Both micrographs located in the left and center column, show the crystal direction along the rolling direction (RD) by the color code according to the inverse pole figure (IPF) displayed as inset. On the right-hand side of this compilation, the kernel average misorientations (KAM) of each measured point is reflected in so-called KAM maps, taking into account first neighbor disorientations. The position of these regions (with even higher magnification) is highlighted in the overview maps as well, using blue-white lines.

In general, the micrographs displayed in Fig. 3 reveal very fine microstructures for all materials covered by the present study.
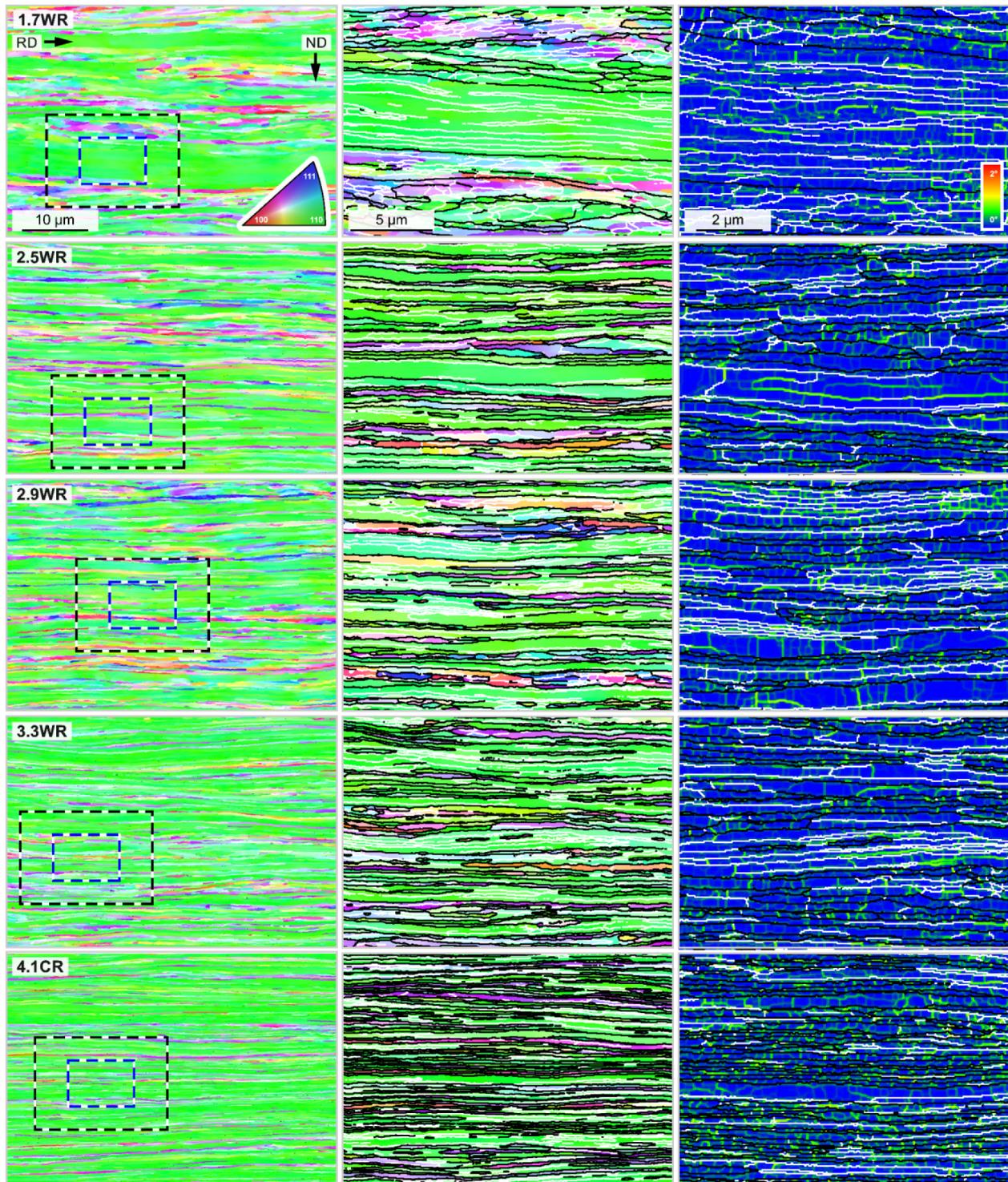
Fig. 3. Microstructural evolution with increasing strain. The orientation maps (left and center column) show the crystal direction along the rolling direction (RD) according to the inverse pole figure (IPF) displayed in the inset. High-angle boundaries with a disorientation angle above a threshold value of 15° are highlighted in black, low-angle boundaries (2°–15°) are represented by white lines (only in the column at the center and right-hand side). In the right column, kernel average misorientation (KAM) maps are displayed showing the substructure by considering disorientation angles below 2°. The given legend shows the color code for the KAM maps displaying KAMs between 0° and 2°. Only the first neighbors were considered. Additionally to the procedure described in the method section for the calculation of the KAMs, also a three-iterations Kuwahara filter was applied for adaptive noise reduction, cf. Ref. [83–85].

Furthermore, the grains possess an anisotropic shape, highly elongated along the rolling direction and, on the other hand, very short grain dimensions along the normal direction, indicating a pancake-like grain morphology. We selected the line intercept method to determine the mean spacing between intersection points along the main sheet directions with HABs and LABs. In this work we provide both results, the prepend values are related to the cross-section defined by the rolling direction and normal direction followed by a bracketed value that refers to the cross section defined by the transverse direction and the rolling direction. If the mean spacing of HABs is considered, all materials can

Table 3

Summary of the microstructural properties. For each material condition and microstructural property, two values are given. The values written in the first row are related to EBSD scans of the cross-section defined by the rolling direction (RD) and the normal direction (ND) of the sheets. The second row (values in brackets) represents the results derived from the scans of the cross-sections defined by transverse direction (TD) and the ND. This applies for the properties: mean spacing between HABs along ND and mean spacing between all boundaries ($\bar{d}_{HAB}$, $\bar{d}_{all}$), the surface density of HABs and the surface density of all boundaries ($\bar{S}_{V,HAB}$, $\bar{S}_{V,all}$), and the fractions of HABs, LABs and CSL boundaries ($\bar{x}_{HAB}$, $\bar{x}_{LAB}$, $\bar{x}_{CSL}$). The fraction of CSL boundaries include all CSL boundaries from Σ3 to Σ25 which are also included in the fraction of high-angle boundaries. Brandon's criterion was applied [86]. For the aspect ratio of grains and the aspect ratio of subgrains ($\bar{r}_{HAB}$, $\bar{r}_{all}$), the number of the first row gives the elongation of the grains and subgrains parallel to RD expressed as times the mean boundary spacing along ND. The aspect ratios written down in the second row describe the elongation parallel to TD. For calculating the aspect ratios the mean values for the boundary spacings along ND were used generated by the result from the cross-sections defined by the RD and the ND and by the TD and the ND as well. Errors represent the standard deviation between the mean values of the four single maps. Dislocation densities determined by the modified Williamson-Hall (mWH) method were taken from an earlier publication [71].

Material	$\bar{d}_{HAB}$/μm	$\bar{d}_{all}$/μm	$\bar{r}_{HAB}$/-	$\bar{r}_{all}$/-	$\bar{S}_{V,HAB}$/μm^{-1}	$\bar{S}_{V,all}$/μm^{-1}	$\bar{x}_{HAB}$/-	$\bar{x}_{LAB}$/-	$\bar{x}_{CSL}$/-	ρ_D/10^{14} m^{-2}
1.7WR	0.811 ± - 0.021(0.8-35 ± 0.0-26)	0.382 ± - 0.016(0.3-60 ± 0.0-32)	4.3(3.3)	4.3(3.2)	1.96 ± 0-.07(2.0-1 ± 0.06)	4.21 ± 0-.11(4.3-5 ± 0.24)	0.47 ± 0-.01(0.4-6 ± 0.02)	0.53 ± 0-.01(0.5-4 ± 0.02)	0.05 ± 0-.00(0.0-5 ± 0.01)	1.1
2.5WR	0.547 ± - 0.051(0.4-62 ± 0.0-33)	0.272 ± - 0.017(0.2-68 ± 0.0-03)	5.8(3.7)	6.5(4.0)	2.93 ± 0-.13(3.1-9 ± 0.15)	5.24 ± 0-.22(5.1-6 ± 004)	0.56 ± 0-.03(0.6-2 ± 0.03)	0.44 ± 0-.03(0.3-8 ± 0.03)	0.06 ± 0-.01(0.0-7 ± 0.01)	1.0
2.9WR	0.397 ± - 0.023(0.3-76 ± 0.0-10)	0.236 ± - 0.011(0.2-26 ± 0.0-05)	7.8(5.2)	7.5(4.7)	3.64 ± 0-.20(3.8-8 ± 0.07)	5.80 ± 0-.23(6.0-3 ± 0.12)	0.63 ± 0-.02(0.6-4 ± 0.01)	0.37 ± 0-.02(0.3-6 ± 0.01)	0.07 ± 0-.00(0.0-7 ± 0.00)	0.5
3.3WR	0.312 ± - 0.016(0.3-15 ± 0.0-16)	0.201 ± - 0.004(0.1-87 ± 0.0-13)	7.6(5.2)	8.3(5.3)	4.39 ± 0-.14(4.6-8 ± 0.34)	6.57 ± 0-.15(7.1-7 ± 0.51)	0.67 ± 0-.01(0.6-5 ± 0.00)	0.33 ± 0-.02(0.3-5 ± 0.00)	0.07 ± 0-.00(0.0-7 ± 0.00)	0.9
4.1CR	0.255 ± - 0.005(0.2-49 ± 0.0-12)	0.159 ± - 0.002(0.1-57 ± 0.0-04)	12.2(6.8)	12.0(6.1)	5.49 ± 0-.13(5.7-1 ± 0.22)	8.11 ± 0-.03(8.3-1 ± 0.17)	0.68 ± 0-.01(0.6-9 ± 0.01)	0.32 ± 0-.02(0.3-1 ± 0.02)	0.08 ± 0-.01(0.0-8 ± 0.00)	8.8

be classified as ultrafine-grained (UFG), i.e. have on average a HAB spacing in the submicron regime [82]. Striking features of the microstructures are addressed in more detail hereinafter.

The microstructure of material 1.7WR has an inhomogeneous character. A vast majority of the grains are oriented $\langle 110 \rangle$ parallel to the rolling direction, indicating that the sheet is highly textured. The structure of these grains belonging to the α-fiber gives the material a band-like character. The $\langle 110 \rangle$-oriented grains surround smaller agglomerations of grains that have distinct different orientations (are not colored in green). Within of some regions that belong to a band of α-fiber orientations, the spacing of HABs along ND is significantly larger than in neighbored regions or as the mean spacing of HABs. One of these bands is displayed in higher magnification in Fig. 3. The selected band has a thickness of approximately 5 μm compared to 0.81 μm (0.84 μm) which is the mean HAB spacing along the normal direction for 1.7WR, cf. Table 3. In this band, most of the boundaries are LABs. Considering all boundaries instead of only HABs, the distribution of boundary spacing reveals a relatively homogenous subgrain structure, which conflicts with the impression derived in the beginning. Same applies to the distribution of boundaries with disorientation angles below 2°, as is indicated by the KAM map of W1.7.

The distribution of HABs in material 2.5WR is quite more homogenous than observed for 1.7WR. Larger bands that are only subdivided by LABs (as described for 1.7WR above) are reduced in thickness and have almost disappeared. As a consequence of an increase in strain by logarithmic 0.8, the mean spacing between HABs along the normal direction and between all boundaries are reduced, possessing mean values of 0.55 μm (0.46 μm) and 0.27 μm (0.27 μm), respectively. During the further passes of warm rolling, the aforementioned tendencies continued further, cf. Table 3. However, in comparison to the first warm rolling steps, the achieved reduction of the mean boundary spacing is much less pronounced for material 2.9WR and 3.3WR. For these materials, we determined mean values considering the spacing of HABs of 0.40 μm (0.38 μm) and 0.31 μm (0.32 μm), respectively. Considering all boundaries, mean boundary spacings along the normal direction of 0.24 μm (0.23 μm) and 0.20 μm (0.19 μm) were determined. Also, the texture of these materials remained dominated by $\{hkl\}\langle 110 \rangle$ orientations. Wide regions of 3.3WR exhibit a distinct bamboo structure [79], i.e. two approximately parallel boundaries (usually HABs) are aligned parallel to the rolling direction and are linked by short boundary segments with smaller disorientation angles.

For material 4.1CR, an additional pass of cold rolling was applied to a section of 3.3WR. In 4.1CR, the bamboo structure is fully developed and we can observe a further grain size reduction along the normal

direction. By that, 4.1CR reaches the minimum values for the mean boundary spacing of all investigated materials in this study with 0.26 μm (0.25 μm) and 0.16 μm (0.16 μm), respectively. Simultaneously, during cold rolling also the aspect ratios have further increased. With an elongation along the rolling directions which measures 12x mean boundary spacing along the normal direction, material 4.1CR possesses by far the highest anisotropic grain morphology.

With increasing strain conducted by warm rolling, the surface density of boundaries increases as well and more and more of these boundaries exhibit high-angle character. To give numbers: After the first step of warm rolling, the surface density of HAB and all boundaries on the cross-section defined by the rolling direction and the normal direction is 1.96 μm^{-1} (47%) and 4.21 μm^{-1}, respectively. These boundary densities further increase to 4.39 μm^{-1} (67%) and 6.57 μm^{-1} during warm rolling as measured for material 3.3WR. For a detailed description of the intermediate rolling steps please cf. Table 3. Material 4.1CR possess the highest surface densities of 5.49 μm^{-1} (68%) and 8.11 μm^{-1}. In contrast to the increasing densities of HABs and all boundaries, the surface density of LABs remains almost constant, and even shows for both investigated cross-sections equivalent values of 2.23 ± 0.06 μm^{-1} (RD × ND) and 2.24 ± 0.20 μm^{-1} (TD × ND) considering the warm-rolled materials. At first glance, also the cell structure (here, boundaries below 2° disorientation) remained unchanged, often developed as boundaries that are aligned parallel to the normal direction and subdividing the highly elongated grains into shorter domains.

It is interesting to note that during cold rolling the total density of boundaries has increased as well, but the fraction of HABs and LABs remained unchanged. During the previous steps of warm rolling, an ongoing increase of the fraction of HABs was observed, which was originated in an almost constant density of LABs. The cold-rolled sheet possess a raised LAB density in comparison to the warm-rolled sheets, however, also maintaining the almost isotropic characteristic, i.e. 2.62 μm^{-1} and 2.60 μm^{-1}, respectively. Although the pancake-like grain morphology with pronounced grain elongation parallel to the rolling direction (between 1.3x and 2.0x the elongation along the transverse direction) suggests the highest surface densities of HABs for the TD-RD cross-section, the determined densities vary only very little, whereby material 4.1CR possess only a difference of 4%. This allows to develop the above statement about a HAB dominated microstructure to a more precise description: the microstructure is determined by prevailing HABs that are aligned parallel to the rolling direction.

The angular distribution of the boundaries is studied in-depth, hereinafter. In Fig. 4a, the surface density (S_V) is plotted against the
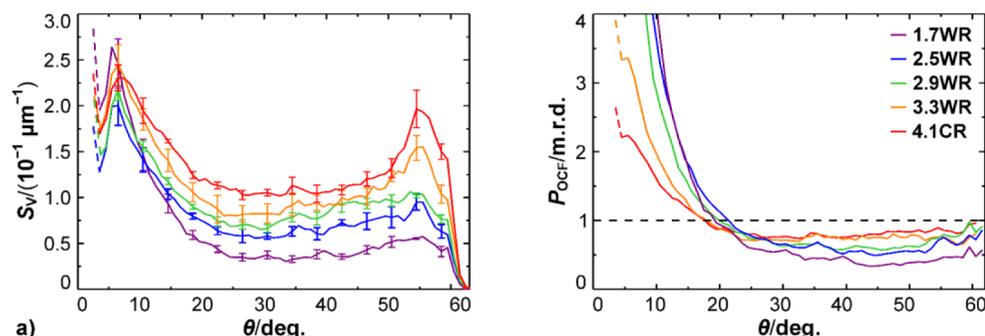
Fig. 4. Angular distribution of boundaries and the impact of the deformation structure. In subplot (a) the surface density of boundaries (S_V) is displayed against the disorientation angle (θ), whereby boundaries below 2° are not included in this consideration. The legend provides information on the allocation of colored graphs to the respective material condition. The surface density is plotted using a binning of 1°. For better readability, however, only every fourth error bar is displayed. The error bars were calculated by comparing the surface density of the single maps (at the respective disorientation angle) recorded for the same material and show the standard deviation. In (b) the respective orientation correlation functions (OCF) are shown (see text for explanation). Similar to subplot (a), in (b) the angular regime above 2° is illustrated. Probability densities are expressed as multiples of random distribution (m.r.d.). Selected binning for plotting was 1° as well. For subplot (a) and (b) both, the displayed data are acquired on the cross-section defined by the transverse direction and normal direction. Dashed lines on the left-hand side of both diagrams reflect disorientations that are not clearly related to boundaries since the high defect density in these materials results in small uncertainties during indexing of the EBSPs [89].
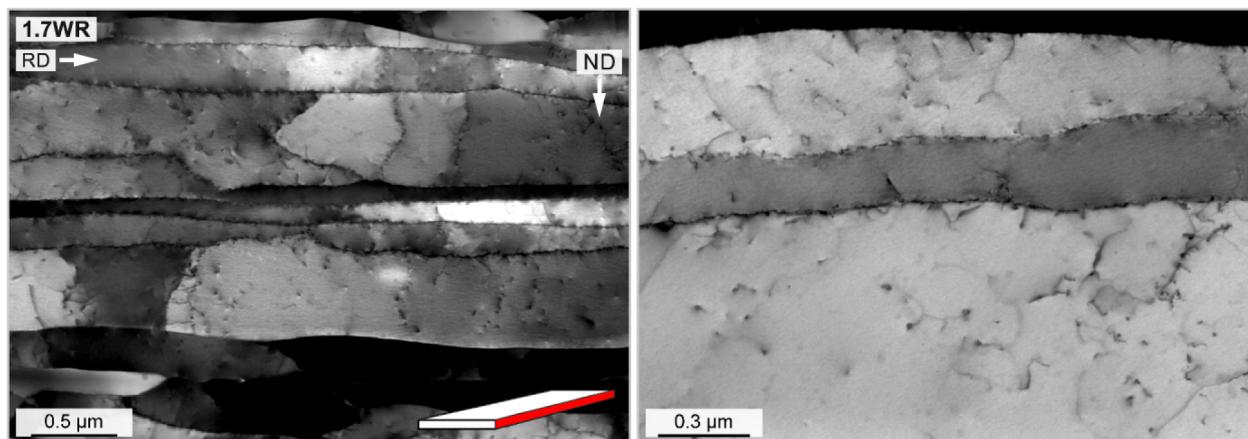
Fig. 5. Subgrain and dislocation structure of material 1.7WR. The ECCI micrograph was taken with inverted signal processing of the BSD detector, i.e. instead of the dark grains, the bright grains are in or close to channeling conditions. The red surface of the inset highlights the scanned cross-section. (For interpretation of the references to color in this figure legend, the reader is referred to the web version of this article.)

disorientation angle (θ), whereby integration of the area below the single curves gives the surface density of all boundaries (to be precise above 2° disorientation) as listed in Table 3. An investigation of the graphs reveals the presence of two pronounced peaks. The first peak indicates a raised frequency of LABs within the angular regime between 5.5° and 6.5°. This peak can clearly be identified for all materials and the maximum of surface density is observed in this angular regime for all materials. The angular resolution of the applied Hough-based approach for orientation determination via EBSD does not allow a quantification of a possible peak shift that might take place during rolling. While the peak density in the LAB regime changes only in a random manner with increasing strain, there is a clear tendency for a growing density of boundaries with a disorientation angle of around 55°. For the materials related to a logarithmic strain of 2.9 and below, the surface density at 55° does not stand out clearly among neighbored disorientation angles. For material 3.3WR and 4.1CR, however, there are no doubts about the existence of this second peak for higher strained W.

The graphs displayed in Fig. 4a are derived from the disorientation angles between directly neighbored pixels [87], which is, in fact, the correlated misorientation function (also known as MODF or MDF) multiplied by the total surface density of all boundaries. Dividing the correlated misorientation function by the respective uncorrelated misorientation function (OODF) gives access to the so-called orientation correlation function (OCF). The orientation correlation function describes a texture-reduced probability density function referring to a not deformed material condition, please cf. Ref. [87] for more details. By this procedure, the frequency of boundaries originated in the deformation structure can be assessed separately, due to elimination the impact of the texture. This differentiates the OCF from the MODF, where the impact of the deformation structure is superimposed with the evolution in texture. We provide the Python script used for the creation of maps with a random positions on the base of the measured EBSD maps as supplementary material. The outcoming OCF-graphs are displayed in Fig. 4b showing the probability density of boundaries (P_{OCF}) with a certain angle against the disorientation angle (θ). Please note, due to the above-outlined procedure, the areas below the curves in an OCF are not equal anymore, as they do in the MODF or OODF plots. A polycrystalline, undeformed material with a uniform density of the grain orientations is expected to generate an angular-independent function with a constant probability density of 1 m.r.d. (multiples of random distribution; or multiples of uniform density [88], to be more precise). This level is highlighted in Fig. 4b by a horizontal dashed line and acts as a reference during the further elucidations. Up to disorientation angles of about 20°, all materials show a strong deviation from the reference line towards higher frequencies due to the presence

of a subgrain structure. This deviation is most apparent for the materials with lower strains. Material 3.3WR and 4.1CR possess a far less dramatic deviation from the reference in the LAB regime, having maximums of 2.2 and 2.7 m.r.d. instead of 10 m.r.d. or higher. Similar to the graphs displayed in Fig. 4a, in Fig. 4b the peak densities are located in the angular regime of 5.5° to 6.5° disorientation.

During the largest parts of the HAB regime (in this work defined to start at 15° disorientation) the curves of all materials are practically parallel to the dashed line, however, they are placed slightly below. They are placed the lower, the less the amount of pre-deformation. This trend is also an effect of the presence of the subgrain structures induced during plastic deformation, in contrast to the deformation-free material condition this concept has as assumption. The almost horizontal evolution of the graphs in the HAB regime demonstrates that neither warm rolling nor cold rolling of W leads to a preferential development of distinct neighborhood relations within the deformation structure. Consequently, the presence of a notable number fraction of coincidence site lattice (CSL) boundaries can be ruled out by an analysis of provided probability density functions. Moreover, in contrast to Fig. 4a, in the texture-reduced probability density functions, the peak around 55° has disappeared, showing that this feature has its origin in the formation of a distinct rolling texture. The presence of this peak (in the MODF) is very likely the consequence of a high orientation density in rotated cube component and γ-fiber orientations [71].

As a supplement to the EBSD based investigations, the evolution of the microstructure is discussed in the following by utilizing ECCI micrographs. We picked the method of ECCI, since ECCI allows imaging the dislocation structures on bulk samples via SEM BSD, while sample preparation by a classic TEM route via electrochemical thinning (e.g. by Tenupol) was not applicable for the below discussed cross-section due to the thin thicknesses of the studied sheets. Alternatively the production of TEM lamellas by FIB milling would be practicable, however, causing a bombardment of Ga ions and, in consequence, extensive so-called FIB damage of the material volume that is in focus of interest [90]. The high density of FIB-induced point defects impedes the clear study of dislocations and other lattice defects to a large extend, cf. e.g. Ref. [91]. In Fig. 5 the microstructure of the less deformed material 1.7WR is shown. Both images were acquired on the RD-ND cross-section highlighted in the inset. The micrographs confirm the impressions gained by EBSD. Material 1.7WR possesses an inhomogeneous (sub-) grain structure with highly elongated grains along the rolling direction (center region of the left-hand side micrograph). These grains coexist with grains that have a larger boundary spacing along the normal direction and lower aspect ratios. The latter consist of several domains, divided by boundaries composed of individual dislocations. Beside the
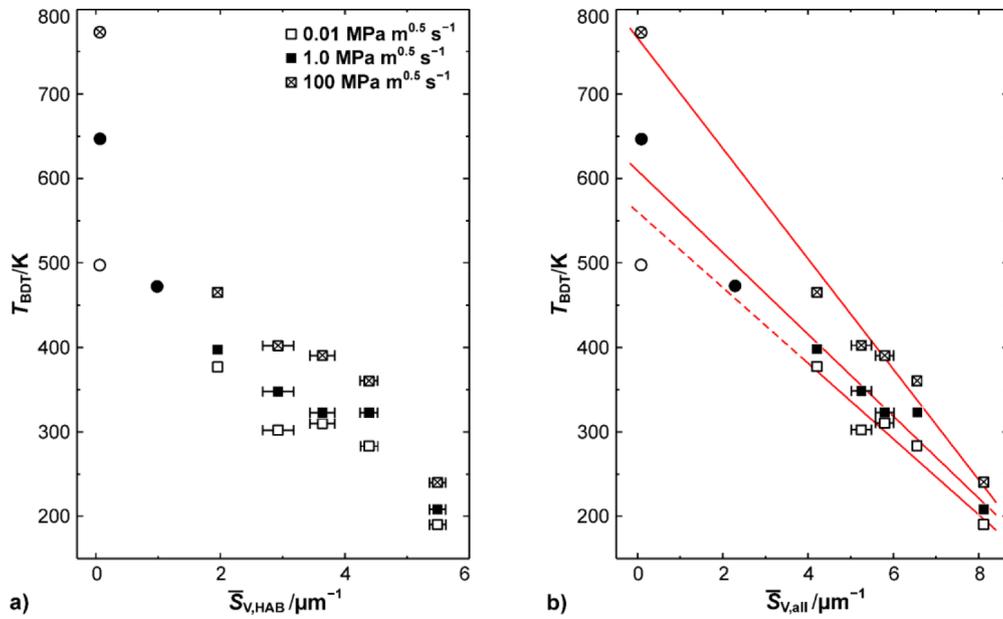
Fig. 6. Microstructure of material 4.1WR and orientations of the analyzed grains. The physical image contrast of the ECCI micrograph is inverted. The red surface of the inset highlights the scanned cross-section. Orientation information concerning the analyzed grains (1) and (2) are reflected by the stereographic projection. Dots showing the points related to crystallographic directions. Red solid and dotted lines display the expected traces of selected ⟨111⟩ dislocation lines. The cubes attached to the stereographic projections display the orientation of the cubic unit cell in the analyzed grains based on EBSD data. Electron backscatter patterns (EBSPs) were generated using the Bruker's ESPRIT DynamicS package. (For interpretation of the references to color in this figure legend, the reader is referred to the web version of this article.)

progress of subdivision by the development of dislocation boundaries, in the forming domains, also a high amount of individual dislocations or forest dislocations can be observed at higher magnification. Several intersection points on the sample surface indicates a significant fraction of not visible dislocation lines

In addition, an in-depth analysis of material 4.1CR was carried out, revealing changes in grain morphology and dislocation structures. While the micrographs of material 1.7WR exhibit only sporadically grains with high aspect ratios, Fig. 6 shows that severely rolled W possesses a lamellar microstructure. Most of these grains span over the whole width of the scanned area. The grains in the material 4.1CR show rather strong lattice rotations, such that only small areas with sharp 2-beam diffraction contrast and therefore proper dislocation visibility are observable. Consequently, an appropriate determination and comparison of dislocation densities require the evaluation of a larger area in 2-beam diffraction contrast, which is the subject matter of future work. It is worth mentioning that after cold rolling a striking fraction of the dislocation lines is running from one horizontal boundary to another in a strictly straight manner. Furthermore, if the dislocations of a single grain are studied separately, the alignment of the segments reveals a few preferred angles of inclination. This fact is elucidated hereinafter more in detail.

We obtained indications about the crystallographic orientation of these straight segments by linking BSD image and EBSD signal. The obtained orientation information is reflected by the displayed units cells in Fig. 6, revealing that the grain, labeled as (1), is slightly off from an ideal γ-fiber orientation and that grain (2) is close to the so-called rotated cube component as the most prominent part of the α-fiber. This gives insights to grains with very common crystal orientation for rolled W [71]. Pleased note, that due to a previous calibration of measured crystal orientation via EBSD detector and obtained electron backscatter pattern (EBSP) gained by a BSD detector, minor offsets between both acquisition systems were compensated, allowing to discuss the crystal orientations linked with features of an ECCI micrograph. With knowledge about the crystal orientation of grain (1) and grain (2), the software T.O.C.A. [80] was utilized to generate the stereographic projections, including relevant crystallographic directions with respect to the measured grain orientations. In a subsequent step, the traces of possible ⟨111⟩ dislocation lines were drawn (red lines) and parallel translated into the ECCI micrograph, allowing to compare predicted traces and the inclination of the marked dislocation lines. As Fig. 6 illustrates, there is, for some of the dislocations, a good match of constructed traces and

visible dislocation lines. This may indicate that these dislocation lines are pure screw segments with Burgers vector ½⟨111⟩. There are, however, also dislocations (in particular in grain 2) whose trace does not coincide with any ⟨111⟩ direction. Note, in any case, that a trace analysis of dislocation lines is rather inaccurate, as the inclination of the dislocation with respect to the surface cannot be properly deduced from the ECC images and is, furthermore, not crystallographically well-defined.

4. Discussion

In this section, we primarily focus on empirical relationships between BDT temperature and boundary-related properties. These relationships are discussed later on in the background of the dualism of boundaries, which act as a dislocation source on the one hand but also confine the mobility of dislocations by causing a pile-up on the other hand. However, in the beginning, we like to make some remarks on the microstructural results.

As a result of the work of Kurishita et al. [92] on molybdenum and later work on coincidence site lattice (CSL) boundaries in W by Mikhailovskij et al. [93], possible contributions of CSL boundaries to improvements in plasticity and resistance against fracture are frequently discussed nowadays, e.g. Ref. [94–96]. In the present work, the frequency of CSL boundaries was calculated as well, cf. Table 3. Our results reveal a slight increase in the fraction of CSL boundaries with increasing strain. With a span from 5% to 8%, the observed fractions are in the expected region of about 8% of all boundaries (considering Σ3 to Σ25 boundaries) if a polycrystal with uniform grain orientations is taken as a reference [97]. If instead a polycrystal with fiber texture is used for comparison purposes, the determined fractions of CSL boundaries are in fact lower than the simulation-derived values [97]. Taking into account the probability densities of the orientation correlation function (OCF) within the HAB regime (Fig. 4b), the absence of distinct peaks also confirms additionally that the above cumulative result also applies for each of the single CSL disorientations. Appreciating these facts, we conclude, that during warm and cold rolling of W no preferred development of CSL boundaries takes place. Furthermore, we like to highlight that the fraction of CSL boundaries using Brandon's criterion ($\Sigma^{-1/2}$) [86] for defining the tolerance limits is known to include several boundaries without special properties [98]. Applying a more rigorous limit by considering a $\Sigma^{-5/6}$ dependence [85], reduces the fractions given in Table 3 by a factor about six on average. Taking into

Fig. 7. Correlation between BDT temperature and the mean surface density of boundaries. In diagram (a) BDT temperatures (T_{BDT}) are plotted against the surface density of HABs ($\bar{S}_{V,HAB}$).considering boundaries with disorientation angles above 15°.The different fillings of the symbols reflect the application of three loading rates (dK/dt) during the experimental campaigns (see legend). Data points plotted as a circle are taken from Ref. [4,109]. Error bars show the standard deviation calculated analyzing the mean values of the multiple maps acquired for each material. In (b), the surface densities of all boundaries ($\bar{S}_{V,all}$) are taken into account, i.e. disorientation angles of 2° and above.

account their low fraction (about 1% if the latter criterion is taken into account), the contribution of CSL boundaries to the rolling-induced reduction in BDT temperature appears to be negligible in the present work.

A comparison of the ECCI micrographs obtained from the warm-rolled material condition (Fig. 5) with the cold-rolled material (Fig. 6) reveals a change in dislocation structures. While after warm rolling predominantly tangled and randomly shaped dislocation lines prevail, the grain interiors of the cold-rolled microstructure exhibit a striking fraction of straight dislocation lines that span across the grains. If a single grain is studied, these straight dislocation lines exist under very few angles of inclination only. The constructed traces, which are expected for ⟨111⟩ dislocation lines match very well the projection of some of the straight dislocation segments indicating that these striking dislocation lines are presumably ½⟨111⟩ screw type. However, since the angle of inclination of the dislocation line concerning the specimen surface cannot be specified by ECCI, we have to point out that this method does not provide indubitable results. On the other hand, for metals with a bcc crystal structure, the Burgers vector is well established to be ½⟨111⟩ type [99] except for short junctions [70]. This applies at least for non-irradiated conditions [100]. This reduces significantly the uncertainty arising due to the remaining degree of freedom and strengthens the above statement about the nature of the straight dislocation segments.

Long, straight screw dislocations are known for cold-deformed W single crystals, cf. Ref. [40,101]. However, the dislocations lines extend over a region that is almost one order of magnitude larger than available between the parallel boundaries of a bamboo-like microstructure. Caillard [101] has linked the straight shape of the screw dislocations with the athermal transition temperature of W [102], which is strain rate-dependent and under quasi-static loading at around 800 K [103]. Above the athermal transition temperature (not to be confused with the BDT temperature), the screw dislocations are curved and highly mobile. Below, the glide of the ½⟨111⟩ screw dislocation requires thermal activation, and the mobility is highly reduced [104]. In contrast to this, non-screw segments retain their high mobility leaving behind straight segments of less mobile screw segments after the expansion of a

dislocation loop [102]. We conclude that the presence of straight segments of presumably screw type in the cold-rolled specimen appears to be related to the reduction in rolling temperature rather than a result of the high plastic strain, which material 4.1CR was exposed to.

In this second part, relationships between the density of boundaries and the BDT temperature are discussed. In his review about the deformation behavior of W at low temperatures, Stephens [105] has shown that the BDT temperature reaches its maximum at a mean grain diameter of about 100 μm. In the regime incorporating smaller diameters than related to the maximum, the BDT temperature often follows a Hall–Petch-like relationship, cf. [5] for a more comprehensive treatment. However, in severely rolled W, a description of the grain dimensions by a single value seems to be an inappropriate attempt since the pancake-like grain morphology in these materials is not reflected. Furthermore, the approach above is not suited to describe the anisotropic nature of the BDT temperature of severely rolled W sheets as frequently reported, e.g. [69,106,107]. For complex materials, a commonly accepted description of the BDT temperature by a given set of microstructural properties is not available so far. Considering the fact that even in room-temperature ductile W with UFG microstructure the BDT is still controlled by the mobility of the screw dislocation [4], we infer the existence of a single set of microstructural parameters, which allows a consistent description of the BDT temperature of monolithic (unalloyed) W materials. This formulation should be able to cover coarse-grained microstructures up to grain sizes of about 100 μm, where presumably the base of crack tip plasticity changes, as suggested by Reiser et al. [108]. In the same manner, this formulation should predict correct BDT temperatures for UFG material conditions on the other hand.

A good correlation between BDT temperature and the mean surface density of HABs have been reported by Ratliff et al. [43] in their research on possible candidates for ductile W sheet alloy, expressing the influence the mean surface density of HABs ($\bar{S}_{V,HAB}$) on the BDT temperature (T_{BDT}) of their materials as

$$T_{BDT} = T_1 - A_1 \bar{S}_{V,HAB} \tag{1}$$

where T_1 and A_1 are constants. For Fig. 7a, this relationship was adopted

for data presentation. In addition to the BDT temperatures determined in the present work (results for three loading rates are displayed), Fig. 7 also contains information from recent works, carried out using an identical experimental setup. These data are related to worked and subsequently heat treated W sheets with technical purity having recovered [109] and recrystallized [4] microstructures, respectively. For easy discrimination, both annealed material conditions are represented by circles instead of squares as used for the as-rolled conditions. At first glance, the attempt illustrated by Fig. 7a reveals a clear trend showing a decrease in BDT temperature with increasing surface density of HABs. However, this attempt does not provide a wide-ranging relationship as was aimed. This statement is primarily based on the presence of discontinuities, whereby the first is located at the transition from recrystallized W to the warm-rolled sheets (left-hand side). A second drop can be identified at the change of the rolling condition from warm to cold working (right-hand side). In diagram Fig. 7a, solely in the regime between $2.0\,\mu m^{-1}$ and $4.4\,\mu m^{-1}$ the derivation of a linear trend line could be justified. This regime contains the warm-rolled sheets. Recrystallized W sheets ($0.01\,\mu m^{-1}$) and cold-rolled W sheets ($5.5\,\mu m^{-1}$) are out of the range of validity.

An improved description was obtained applying (Eq. (1)) but using the mean surface density of all boundaries ($S_{V,all}$) instead of considering HABs only. Similar to the previous attempt, in Fig. 7b the BDT temperature is plotted against the selected microstructural property. In particular, a good agreement between shown trend lines and data points can be attested for the crossed and filled symbols, exhibiting deviations between trend an experimental result of about maximal 20 K only (considering BDT temperatures that span over a range of about 500 K). Both data sets represent the BDT temperatures determined by applying an intermediate ($1.0\,MPa\,m^{0.5}\,s^{-1}$) and a fast loading rate ($100\,MPa\,m^{0.5}\,s^{-1}$), respectively. After evaluating the data that are related to the loading rate of $0.01\,MPa\,m^{0.5}\,s^{-1}$, the impression of more scattering results is gained in general but in particular for the recrystallized material condition (left-hand side). This is very likely an effect of the lower number of fracture toughness tests that were carried out due to test durations of several hours at this loading rate.

At this point, however, we have to mention that the above attempts based on the surface density are subjected to relevant restrictions in describing the BDT temperature as an anisotropic property. Since the surface density is an area property, some variations of the crack system cannot be represented. Considering the basic directions of a rolled sheet RD (L), TD (T), ND (S), for six crack systems (3^2 possible letter combinations minus the three invalid letter pairs LL, TT, and SS) only three cross-sections are available. Consequently, as good as this formulation seems to work for a data set derived from specimens with identical crack system but different material conditions, as bad the property surface density of boundaries is expected to be suited for a comprehensive approach. This is briefly demonstrated hereinafter discussing specimens with identical microstructure but equipped with an L-T and

an S-T crack system, respectively. In Fig. 8 these two crack systems are illustrated. By definition, the direction of crack propagation is parallel to the transverse direction for both crack systems but the respective plane normal to the crack plane is different. Whereas the plane normal in an L-T crack system is parallel to the rolling direction, in an S-T crack system the plane normal points into the normal direction. As a result, the crack front of the first example (L-T) is aligned along the normal direction and of the latter one (S-T) along the rolling direction, cf. Fig. 8. Between both crack systems fracture behavior is strikingly different. While by Nikolić et al. [68] the BDT temperature has been determined to be at about room-temperature for specimens with L-T crack system and prevailing transgranular fractures have been observed, Pfeifenberger et al. [107] have shown that by the selection of a crack system forcing crack propagation in the rolling plane, extreme brittle fracture behavior (intergranular crack path) is obtained although both studies are based on similar materials. This implies for the above example using L-T and S-T crack systems that a suited model needs to predict a lower BDT temperature for specimens with L-T crack system in comparison to experiments with the S-T crack system (for a given material with pancake-like microstructure). This requirement is not fulfilled by (Eq. (1)) since in the above approach both crack systems can be linked with the same cross-section (RD × ND) and in consequence with an identical surface density and, therefore, the same predicted BDT temperature.

To overcome this restriction, the utilization of a direction-dependent microstructural property seems ineluctable. In recent works [7,66], promising results have been obtained using the Hall–Petch-like relationship

$$T_{BDT} = T_2 - A_2 \bar{\lambda}_{HAB}^{-0.5} \tag{2}$$

where T_{BDT} is the BDT temperature, T_2 and A_2 are constants. The quantity $\bar{\lambda}$ is denoted as mean chord length in the following. We define chord length as the boundary spacing along the crack front and distinguish between chord length for HABs and chord for all boundaries considering disorientations above 15° and 2°, respectively. Independent of the related type of boundaries that is taken into consideration (HABs only or instead of all boundaries), in first approximation, a generalized formulation of the direction-dependent nature of chord length ($\bar{\lambda}$) can be expressed as follows

$$\bar{\lambda} = \left| \bar{g} \bar{d}_{ND} \begin{bmatrix} \bar{r}_{RD|ND} & \cdots & \cdots \\ \cdots & \bar{r}_{TD|ND} & \cdots \\ \cdots & \cdots & 1 \end{bmatrix} \right| \tag{3}$$

where g describes the orientation of the crack front in relation to the reference frame of a rolled sheet [74] using a vectorial notation and $\bar{d}_{ND}$ is a scalar quantity representing mean boundary spacing parallel to the normal direction (ND). In (Eq. (3)) the mean spacing between boundaries related to the remaining main directions of a rolled sheet are given
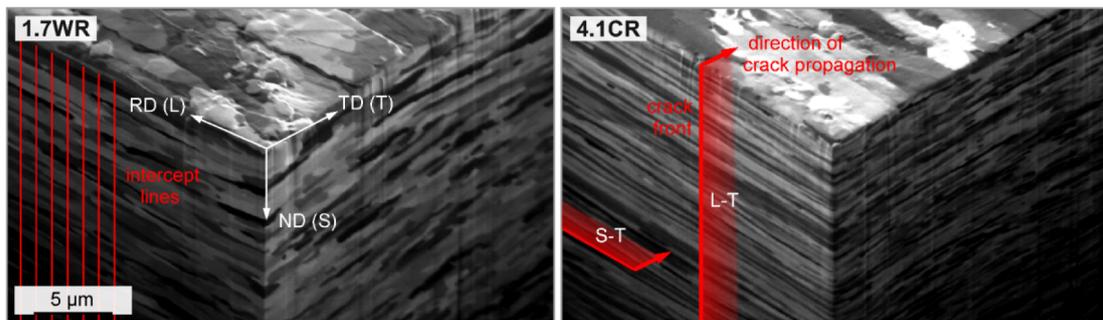

Fig. 8. Elucidation of the quantity chord length and selected crack systems. In addition to the 3D representation of the microstructure of 1.7WR the alignment of the test lines used for determining the property chord length by line intercept method is overlaid. Based on the microstructure of 4.1CR the alignment of the different crack systems is illustrated.
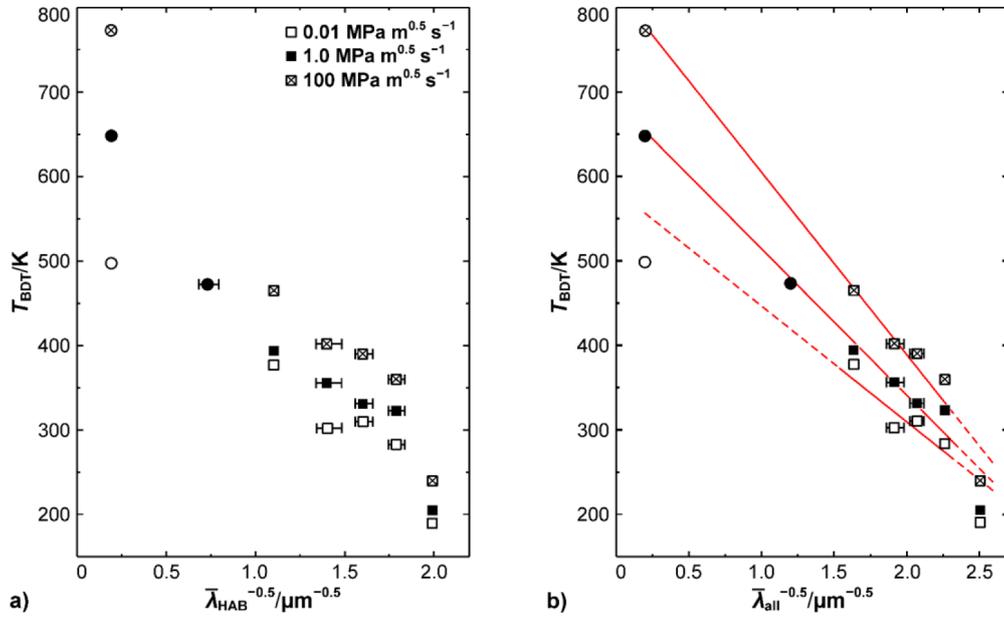
Fig. 9. Correlation between BDT temperature and chord length using a Hall–Petch-like relationship. In diagram (a) BDT temperatures (T_{BDT}) are plotted against the square root of the inversed mean chord length for HABs ($\bar{\lambda}_{HAB}$) considering boundaries with disorientation angles above 15°. The different fillings of the symbols reflect the application of three loading rates (dK/dt) during the experimental campaigns. Data points plotted as square are taken from Ref. [4,109]. Error bars show the standard deviation calculated analyzing the mean values of the multiple maps acquired for each material. In (b), all boundaries ($\bar{\lambda}_{all}$) starting with a disorientation angle of 2° are taken into account.

by the aspect ratios $\bar{r}_{RD|ND}$ (rolling direction) and $\bar{r}_{TD|ND}$ (transverse direction) referring to ND, cf. Table 3. Since in this work solely specimens with L-T crack system were tested, $\mathbf{g}$ can be written as $\langle 0|0|1 \rangle$ further on. As illustrated in Fig. 8, under this circumstance, i.e. only specimens with L-T crack system are utilized, the mean chord length is equivalent to the mean boundary spacing along the normal direction.

In Fig. 9 the suitability of (Eq. (2)) for the available data set is investigated, plotting the evolution in BDT temperature against the inverse square root of the mean chord length for HABs ($\bar{\lambda}_{HAB}$) and against the inverse square root of the mean chord length for all boundaries ($\bar{\lambda}_{all}$), respectively. First subplot (a) is discussed. Again, the BDT temperatures for all three loading rates are displayed, but in the following the main focus remains on the results achieved in the campaigns related to intermediate (filled) and fast loading rates (crossed symbols). In first approximation, for Fig. 9a the same applies as earlier discussed for Fig. 8a: For the warm-rolled sheets the application of a linear trend line can be considered, while predicted BDT temperatures of the cold-rolled material (right-hand side) and the recrystallized material (left-hand side) are clearly over- and underestimated, respectively. Also quite similar to Fig. 8 is the fact, that by the consideration of all boundaries instead of HABs only a better (linear) correlation is obtained as is revealed by Fig. 9b. This statement, however, needs to be restricted to the warm-rolled and annealed materials. The extrapolation of the drawn trend lines to smaller chord length (right-hand side) reveals that this simple Hall–Petch-like approach does not reflect the reduction in BDT temperature during cold rolling in the same magnitude as observed in experiments. Furthermore, a theoretical consideration of this approach reveals that by this single parameter approach, again, only three different BDT temperatures can be described instead of the six independent that are required to cover all basis crack systems. Consequently, an approach with at least two independent microstructural variables needs to be developed.

In order to overcome this limitation, in the following a so-called *extended Hall–Petch-like relationship* is investigated. Reflecting recent simulation-based work by Reiser et al. [108], we propose the following relationship for describing the rolling-induced evolution in BDT temperature by using a more comprehensive approach of the kind

$$T_{BDT}^{mn} = T_3 - A_3 \bar{r}_{x|\lambda}^{0.5} \bar{\lambda}^{-1} \tag{4}$$

where T_{BDT}^{mn} is the BDT temperature related to a crack system mn, whereby in a specific example n and m are replaced by L, T, or S. Furthermore, T_3 and A_3 are constants, $\bar{r}_{x|\lambda}$ represents the aspect ratio defined by the mean boundary spacing along the plane normal to the crack plane in relation to $\bar{\lambda}$, which is the mean chord length (the boundary spacing along the crack front). Data presentation in Fig. 10 was conducted by applying this extended formulation. Due to the fact that in this work solely specimens with L-T crack system were tested, the aspect ratio $\bar{r}_{RD|\lambda}$ is defined by the boundary spacing along the rolling direction divided by the boundary spacing along the normal direction. Evaluation of the data related to HABs only (Fig. 10a) reveals that still both discontinuities in the evolution of the BDT temperature are present. However, compared to Fig. 7a and Fig. 8a, the drop between the warm- and cold-rolled materials seems to be less pronounced. Similar to the earlier tried relationships, a better correlation is achieved if chord length for all boundaries and the aspect ratio related to boundaries with disorientation angles of 2° or above are considered. Utilization of (Eq. (4)) allows a proper description of the rolling-induced decrease in BDT temperature including both the warm-rolled conditions and cold-rolled sheet. Furthermore, also the BDT temperature of the annealed material with a strongly recovered microstructure (single filled circle at $1.98\,\mu m^{-1}$) is pretty well predicted by the trend line. This suggests that the BDT temperature of W sheets scales with the chord length for all boundaries and furthermore with the boundary spacing parallel to the normal of the crack plane. However, this first well-fitting assessment needs to be rethought after evaluation of the match of trend lines and measured BDT temperatures of the recrystallized sheet. While for the materials with prevailing deformation structure (as-rolled and the recovered conditions) the extended Hall-–Petch-like relationship appears very suited, the predicted BDT temperatures of the deformation-free material (left-hand side in Fig. 10b) are far off the actual determined temperatures. This limits the proposed relationship to materials with relevant deformation structures so far. In this scope, however, (Eq. (4)) provides proper predications.

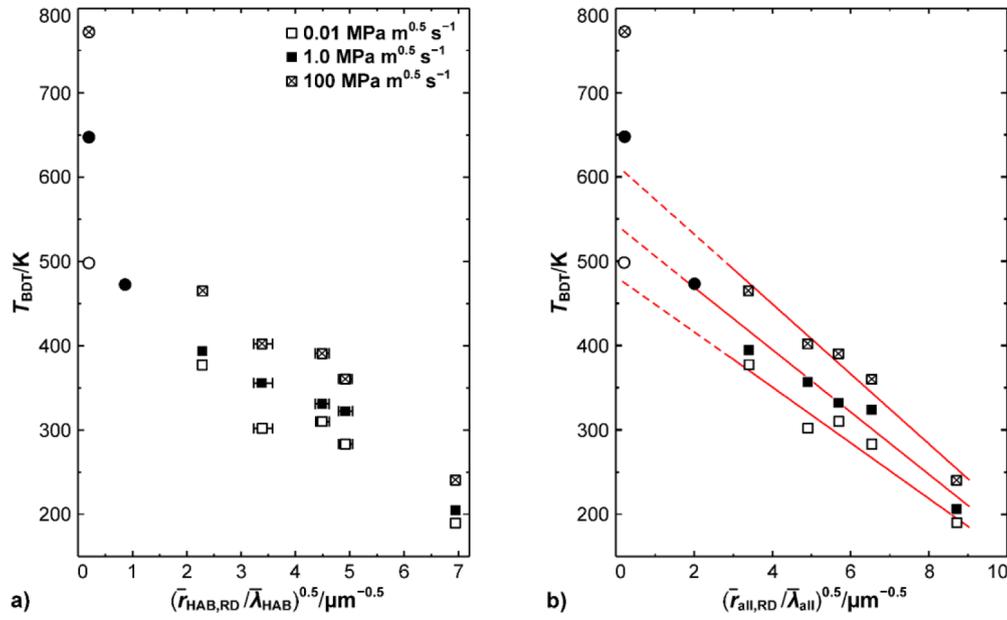Possible reasons for the limitation of (Eq. (4)) to materials with

Fig. 10. Correlation between BDT temperature and chord length using an extended Hall–Petch-like relationship. In diagram (a) BDT temperatures (T_{BDT}) are plotted using the extended Hall–Petch-like relationship considering mean chord length for HABs ($\bar{\lambda}_{\text{HAB}}$) and the aspect ratio for the rolling direction ($\bar{r}_{\text{HAB,RD}}$). The different fillings of the symbols reflect the application of three loading rates (dK/dt) during the experimental campaigns. Data points plotted as square are taken from Ref. [4,109]. Error bars show the standard deviation calculated analyzing the mean values of the multiple maps acquired for each material. In (b), all boundaries ($\bar{\lambda}_{\text{all}}$, $\bar{r}_{\text{all,RD}}$) are taken into account.

deformation structure might be originated in a different character of HABs which have formed by aggregating dislocations during plastic deformation or are the result of recrystallization on the other hand [79]. A detailed treatment of HABs in UFG materials has been provided by *Sauvage et al.* [110] and Wilde [111]. As an additional contributing factor, also dislocation multiplication [112,113] shall be mentioned at this point. Dislocation densities in worked W typically span from 10^{13} to $10^{15}\,\text{m}^{-2}$ [114–116], but after recrystallization the dislocation density is reduced to about $10^{12}\,\text{m}^{-2}$ [117]. As a consequence, the generation of dislocation loops caused by dislocation multiplication appears to be less likely which also might influence the BDT temperature, as shown hereinafter. We also like to mention differences in fracture behavior between the materials that are well-described by the found relationship applied for the drawing of Fig. 10 and the material that underwent recrystallization (all observations gained in tests with L-T crack system only). While the BDT of the first, i.e. the as-rolled and the recovered condition, manifest in a transition from transgranular fracture to ductile behavior, for the fracture of the recrystallized material in the brittle regime intergranular fracture prevails.

In this section, we discuss the outcome of the above correlation attempts in the background recent simulation-derived relationships based on discrete dislocation dynamics (DDD) studies, which is taken as a chance to deduce indications about the relation between microstructure and mechanical behavior. In the numerical study conducted by Reiser et al. [108], the impact of the spatial distribution of dislocation sources and obstacles for the glide of dislocations has been evaluated. As concluding outcome, the relationship

$$T_{\text{BDT}} = T_0 - A d_\delta^{0.5} d_\lambda^{-1} \tag{5}$$

has been derived, where T_{BDT} is the calculated BDT temperature, T_0 and A are constants. The variable d_δ reflects the mean free path for dislocation glide and d_λ is denoted as mean dislocation source spacing along the crack front. This formulation is similar to (Eq. (4)), whereby the approach by Reiser et al. [108] is based on the spatial distribution of functional elements, while the approach discussed in the present work reflects the distribution of boundaries in real existing microstructures. The matching of both approaches indicates that intersecting boundaries

lead very likely to stimulated dislocation nucleation along the crack front improving the shieling of the crack tip and lowering the BDT temperature. Furthermore, we can learn that boundaries out of the notch zone predominantly act as an obstacle for dislocation glide. Nucleation of dislocation at both types of boundaries LABs [79] and HABs [118,119] has been reported in a large number of works and is well-known. Also MD calculations conducted by Tanaka et al. [120] have indicated that HABs act as dislocation sources and that a grain refinement consequently might cause an increase in the number of dislocation sources. In most works only HABs are considered in the discussion of the BDT temperature. As exception we like to mention Ref. [121]. We furthermore like to highlight that the density of intrinsic sources in W is believed to be quite low, cf. Ref. [122,123]. Transferred to conventionally produced, coarse-grained W, we deduce that the low density of intrinsic dislocation sources in combination with a lack of nucleation sites which are preferred to stimulated dislocation nucleation are responsible for the brittle nature of W. Hot-worked W possesses a typical boundary spacing of several microns [124,125].

The data presentation in Fig. 10b suggests that besides the chord length for all boundaries also the mean boundary spacing along the plane normal to the crack plane needs to be taken into account for formulating the impact of the microstructure on the BD temperature. For severely rolled specimens with an L-T crack system, this additional variable is equal to the boundary spacing of all boundaries along the rolling direction, cf. Fig. 8. Considering the continuum-based work by *Reiser et al.* [108], the boundary spacing along the rolling direction scales with the mean free path of dislocation glide. Beyond a continuum model, dislocation glide in W takes place on densely packed crystallographic planes of type {110}, cf. Ref. [126–128]. Due to that, the dominating configuration of the glide planes at the crack tip is also texture-dependent and might influence the direction, which needs to be selected for determining the representative boundary spacing, scaling with the mean free path for dislocation glide. This fact is elucidated by means of Fig. 11 in the following. First, a short recap of the model used by Reiser et al. [108] is given which is basically equivalent to the models proposed by Hirsch et al. [129], Roberts et al. [130], and Hartmaier et al. [131]. In these models for crack tip plasticity,
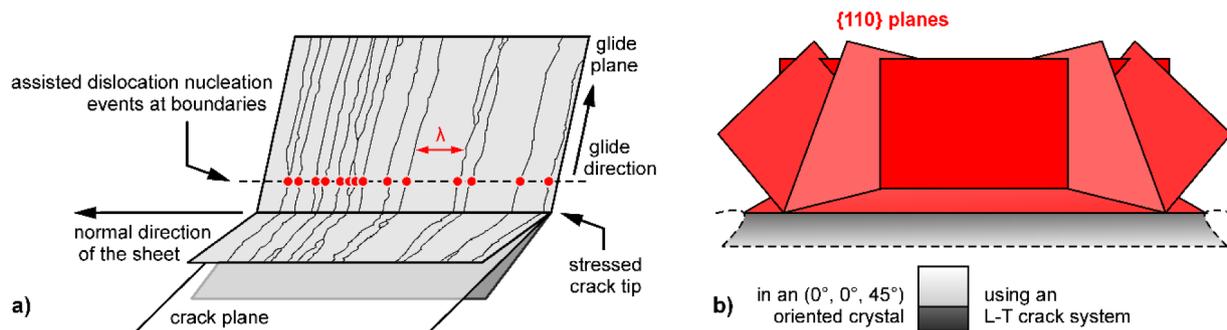
Fig. 11. Possible sites of dislocation nucleation and comparison of glide planes in a continuum vs. bcc crystal. Red full circles highlight suggested sites for stimulated dislocation nucleation events at boundaries (plotted in black) near the crack front. The spacing between boundaries along the crack front is denoted as the chord length. The boundary spacing along the normal direction of the sheet coincidences with the chord length due to the selected L-T crack system of the SECT sample. In the continuum model (a) the angle of inclination between crack plane and glide plane is 72°, while in the (b) the {1 1 0} glide planes are oriented 0° (1x),60° (4x) and 90° (1x) to the crack plane.

dislocation loops nucleate (at a selected critical stress) along the crack front but with some distance to the crack tip as highlighted in Fig. 11a by red markings (drawn boundaries added for highlighting the impact of intersecting boundaries to dislocation nucleation but not considered in the above mentioned models). In a continuum model, the nucleated loops expand in the plane possessing an angle of inclination of 72° to the crack plane [132] since under this angle the highest critical resolved shear stress acts [133]. The half of the dislocation loop that nucleates between the source and the crack tip is attracted by the image force of the free surface. This part of the loop glides towards the crack tip and causes blunting of the crack tip after leaving the material volume. Much more effect on the accommodation of the stresses at the crack tip have the parts of the dislocation loop which are located on the opposite side of the dislocation source, i.e. the parts that glide away from the crack tip. The expansion of the loop leads to the merging of neighbored loops and form a single plane dislocation line. It is important to note that the dislocation lines provide effective shielding of the crack tip first after merging. According to the above-quoted models, a smaller spacing between dislocation sources leads to an earlier merging of the half loops (at a smaller distance to the crack tip) and more effective shielding of the crack tip. We like to highlight at this point that a higher number of dislocation sources do not release a higher density of gliding dislocations after merging the dislocation loops, so that the Taylor model does not explain the improved stress accommodation at given strain rate and test temperature.

As mentioned before, dislocation glide in W takes place in type {1 1 0} glide planes [126]. Reflecting the high orientation density of the rotated cube component severely rolled W [71], in the following, we investigate the alignment of the {1 1 0} planes in front of the crack tip that penetrates a crystal with rotated cube orientation and which is related to an L-T crack. These six {1 1 0} planes are displayed in Fig. 11b (highlighted in red). One glide plane is parallel to the crack plane. The remaining {1 1 0} planes possess a steep angle of inclination relative to the crack plane, spanning angles of inclination of 60° (4x) and 90° (1x). Leaving further lattice defects aside in this basic treatment, the mean free path for dislocation glide is then primarily controlled by the boundary spacing along the direction that is parallel to the direction of the plane normal of the crack plane. This is in agreement with the utilization of the boundary spacing along the rolling direction as suggested above, cf. (Eq. (4)). Furthermore, since similar to HABs, also LABs are assumed to be impenetrable for dislocations (for Al the transition from penetrable to impenetrable is about 3° disorientation [134]), the consideration of all boundaries instead of solely HABs in models for crack tip plasticity seems reasonable and is also supported by the improved correlation in Fig. 10b and both other approaches.

In a nutshell, this work gives strong evidence that a reduced boundary spacing along the crack front is a promising strategy to overcome the brittle nature of W. In addition, our correlation attempts using simulative-derived relationships revealed that also the boundary spacing along the normal of the crack plane influences the measured BDT temperature. While the intersecting boundaries are believed to increase the density of dislocation sources along the crack front and, due to that, enhance the shielding of the crack tip, our correlation attempts suggest a blocking character for the boundaries with a distance to the crack front.

Beside relevant resistance against unstable crack propagation at room temperature (in unirradiated condition), the application of W in a fusion reactor environment also requires a strategy to mitigate irradiation hardening and the related degradation of properties. To improve the irradiation behavior of W, also a UFG microstructure might be beneficial since HABs [135] and dislocation networks [136] are known to represent effective sinks for some radiation-induced defects (and some dispersoids [137] as well). First promising results have been provided by Armstrong et al. [136] and Zhang et al. [138], both comparing irradiation-induced changes in as-worked W and annealed material condition, possessing a recrystallized microstructure with significantly larger grains. In both studies, improved resistance against irradiation hardening was obtained for the as-received material conditions. Neutron irradiation campaigns including room-temperature ductile W (material 4.1CR) are presently performed and will be subject of future publications. If UFG microstructures can mitigate embrittlement under neutron irradiation in a relevant manner, severe rolling (and small Re additions) could proof to be a promising strategy for producing powerful divertor armor materials in large quantities.

5. Conclusions

Recent works on severely rolled W with UFG microstructure have shown that the rate-limiting mechanism controlling the BDT is still the glide of the ½⟨111⟩ screw dislocation, and thus the same as in conventionally produced coarse-grained W. This observation has raised questions, asking for the contribution of the high density of rolling-induced lattice defects to the improvements in transition temperature, enabling even room-temperature ductility. Referring to the main questions outlined in the introduction section, our conclusions can be summarized as follows:

(1) Randomly shaped dislocations and forest dislocations characterize the dislocation structure of the less deformed, warm-rolled specimen. After cold rolling, however, a striking fraction of dislocations span across the grains starting and ending at boundaries that are

aligned parallel to the rolling direction. These dislocation lines have a straight shape and are presumably ½⟨111⟩ screw segments.

(2.1) Empirical relationships between the changing density of boundaries with increasing strain and the related evolution in BDT temperature were revealed. In this work, approaches considering all boundaries instead of HABs solely, provide better descriptions of the rolling-induced shift in BDT temperature.

(2.2) An extended Hall–Petch-like relationship based on the chord length for all boundaries and the aspect ratios of the subgrains appears best suited to describe the evolution in BDT temperature for deformed materials. Out of the three tested relationships this extended formulation has the potential to express entirely the influence of the crack system on the BDT temperature if the grain morphology exhibits a strong anisotropic nature.

(2.3) The good agreement between this simulation-derived extended Hall–Petch-like relationship and our results corroborates the theory suggesting an enhanced shielding of the crack tip by the stimulated nucleation of dislocations at boundaries that intersect with the crack front.

(3) There is no evidence for a preferred development of CSL boundaries during severe rolling of W. In all material conditions and for all investigated cross-sections, the fraction of CSL boundaries meet the statistically expected region, if a polycrystal with uniform distributed grain orientations is selected as reference. In fact, the determined fractions are even lower compared to the results derived from simulated materials with distinct fiber texture.

In summary, an enhanced dislocation nucleation stimulated by the presence of rolling-induced LABs and HABs seems very likely to be responsible for the low BDT temperatures of severely deformed W sheets with UFG microstructure. Shielding of the crack tip is more effective the smaller the mean spacing between dislocation boundaries along the crack front (and the larger the boundary spacing parallel to the plane normal of the crack plane). This work demonstrates that crack tip plasticity and the description of the BDT temperature are very complex. For a comprehensive model of the BDT temperature also the crystallographic texture should be considered determining the alignment of the glide planes in relation to the crack system. In hot-rolled W, the free path of dislocation glide is very spacious. On the other hand, the spacing between sites for a preferred dislocation nucleation along the crack front is typically several microns, which results in a lack of dislocation nucleation sites. This is interpreted as the primary reason for the brittle nature of conventionally produced W materials. However, this lack of dislocation nucleation sites, and therefore the brittleness of W, can be remedied by an UFG microstructure, which even allows gaining room-temperature ductility.

To put the focus on the application of W as plasma-facing material, these findings on UFG W open up the possibility to design reactor components with tailored microstructures that provide a significantly improved resistance against unstable crack propagation. The gained improvement, however, is highly anisotropic if the grain dimensions are anisotropic as well. In such a case, the expected stresses in the component (as a consequence of the operation in the fusion reactor) need to be analyzed carefully, ensuring that the tough orientation of the material matches the preferred direction for crack propagation in the loaded part and in consequence a failsafe operation of the component.

CRediT authorship contribution statement

Carsten Bonnekoh: Project administration, Conceptualization, Investigation, Formal analysis, Writing - original draft, Visualization. **Philipp Lied:** Formal analysis, Writing - review & editing. **Stefan Zaefferer:** Methodology, Software, Investigation, Writing - review & editing. **Ute Jäntsch:** Investigation. **Andreas Hoffmann:** Investigation. **Jens Reiser:** Conceptualization, Supervision, Funding acquisition. **Michael Rieth:** Supervision, Funding acquisition, Writing - review & editing.

Declaration of Competing Interest

The authors declare that they have no known competing financial interests or personal relationships that could have appeared to influence the work reported in this paper.

Appendix A. Supplementary data

Supplementary data to this article can be found online at https://doi.org/10.1016/j.nme.2020.100769.

References

[1] G. Pintsuk, Tungsten as a plasma-facing material, in: R.J.M. Konings, T.R. Allen, R. E. Stoller, S. Yamanaka (Eds.), Radiation effects in structural und functional material for fission and fusion reactors, Elsevier, Amsterdam, NLD, 2012, pp. 551–581. https://doi.org/10.1016/B978-0-08-056033-5.00118-X.

[2] S. Wurster, N. Baluc, M. Battabyal, T. Crosby, J. Du, C. García-Rosales, A. Hasegawa, A. Hoffmann, A. Kimura, H. Kurishita, R.J. Kurtz, H. Li, S. Noh, J. Reiser, J. Riesch, M. Rieth, W. Setyawan, M. Walter, J.-H. You, R. Pippan, Recent progress in R&D on tungsten alloys for divertor structural and plasma facing materials, J. Nucl. Mater. 442 (2013) S181–S189, https://doi.org/10.1016/j.jnucmat.2013.02.074.

[3] D. Stork, P. Agostini, J.L. Boutard, D. Buckthorpe, E. Diegele, S.L. Dudarev, C. English, G. Federici, M.R. Gilbert, S. Gonzalez, A. Ibarra, C. Linsmeier, A. Li Puma, G. Marbach, P.F. Morris, L.W. Packer, M. Rieth, M.Q. Tran, D.J. Ward, S.J. Zinkle, Developing structural, high-heat flux and plasma facing materials for a near-term DEMO fusion power plant: The EU assessment, J. Nucl. Mater. 455 (2014) 277–291, https://doi.org/10.1016/j.jnucmat.2014.06.014.

[4] C. Bonnekoh, J. Reiser, A. Hartmaier, S. Bonk, A. Hoffmann, M. Rieth, The brittle-to-ductile transition in cold-rolled tungsten sheets: the rate-limiting mechanism of plasticity controlling the BDT in ultrafine-grained tungsten, J. Mater. Sci. (2020), https://doi.org/10.1007/s10853-020-04801-5.

[5] J. Reiser, J. Hoffmann, U. Jäntsch, M. Klimenkov, S. Bonk, C. Bonnekoh, M. Rieth, A. Hoffmann, T. Mrotzek, Ductilisation of tungsten (W): On the shift of the brittle-to-ductile transition (BDT) to lower temperatures through cold rolling, Int. J. Refract. Met. Hard Mater. 54 (2016) 351–369, https://doi.org/10.1016/j.ijrmhm.2015.09.001.

[6] A. Wronski, A. Foukdeux, The ductile-brittle transition in polycrystalline tungsten, J. Less Common Metals 8 (1965) 149–158, https://doi.org/10.1016/0022-5088(65)90042-1.

[7] C. Bonnekoh, A. Hoffmann, J. Reiser, The brittle-to-ductile transition in cold rolled tungsten: On the decrease of the brittle-to-ductile transition by 600 K to −65 °C, Int. J. Refract. Met. Hard Mater. 71 (2018) 181–189, https://doi.org/10.1016/j.ijrmhm.2017.11.017.

[8] Y. Mutoh, K. Ichikawa, K. Nagata, M. Takeuchi, Effect of rhenium addition on fracture toughness of tungsten at elevated temperatures, J. Mater. Sci. 30 (1995) 770–775, https://doi.org/10.1007/BF00356341.

[9] E. Tejado, P.A. Carvalho, A. Munoz, M. Dias, J.B. Correia, U.V. Mardolcar, J.Y. Pastor, The effects of tantalum addition on the microtexture and mechanical behaviour of tungsten for ITER applications, J. Nucl. Mater. 467 (2015) 949–955, https://doi.org/10.1016/j.jnucmat.2015.10.034.

[10] E. Tejado, Performance of structural materials for the DEMO divertor. Ph.D. Thesis, Madrid, ESP, 2017.

[11] D. Rupp, S.M. Weygand, Loading rate dependence of the fracture toughness of polycrystalline tungsten, J. Nucl. Mater. 417 (2011) 477–480, https://doi.org/10.1016/j.jnucmat.2010.12.118.

[12] E. Gaganidze, D. Rupp, J. Aktaa, Fracture behaviour of polycrystalline tungsten, J. Nucl. Mater. 446 (2014) 240–245, https://doi.org/10.1016/j.jnucmat.2013.11.001.

[13] S. Nogami, S. Watanabe, J. Reiser, M. Rieth, S. Sickinger, A. Hasegawa, A review of impact properties of tungsten materials, Fusion Eng. Des. 135 (2018) 196–203,

https://doi.org/10.1016/j.fusengdes.2018.08.001.

[14] M. Rieth, S.L. Dudarev, S.M. Gonzalez de Vicente, J. Aktaa, T. Ahlgren, S. Antusch, D.E.J. Armstrong, M. Balden, N. Baluc, M.-F. Barthe, W.W. Basuki, M. Battabyal, C.S. Becquart, D. Blagoeva, H. Boldyryeva, J. Brinkmann, M. Celino, L. Ciupinski, J.B. Correia, A. de Backer, C. Domain, E. Gaganidze, C. García-Rosales, J. Gibson, M.R. Gilbert, S. Giusepponi, B. Gludovatz, H. Greuner, K. Heinola, T. Höschen, A. Hoffmann, N. Holstein, F. Koch, W. Krauss, H. Li, S. Lindig, J. Linke, C. Linsmeier, P. López-Ruiz, H. Maier, J. Matejicek, T.P. Mishra, M. Muhammed, A. Muñoz, M. Muzyk, K. Nordlund, D. Nguyen-Manh, J. Opschoor, N. Ordás, T. Palacios, G. Pintsuk, R. Pippan, J. Reiser, J. Riesch, S.G. Roberts, L. Romaner, M. Rosiński, M. Sanchez, W. Schulmeyer, H. Traxler, A. Ureña, J.G. van der Laan, L. Veleva, S. Wahlberg, M. Walter, T. Weber, T. Weitkamp, S. Wurster, M.A. Yar, J.H. You, A. Zivelonghi, Recent progress in research on tungsten materials for nuclear fusion applications in Europe, J. Nucl. Mater. 432 (2013) 482–500, https://doi.org/10.1016/j.jnucmat.2012.08.018.

[15] J. Reiser, M. Rieth, Optimization and limitations of known DEMO divertor concepts, Fusion Eng. Des. 87 (2012) 718–721, https://doi.org/10.1016/j.fusengdes.2012.02.010.

[16] J. Reiser, M. Rieth, A. Möslang, H. Greuner, Armstrong, David E. J., T. Denk, T. Gräning, W. Hering, A. Hoffmann, J. Hoffmann, H. Leiste, T. Mrotzek, R. Pippan, W. Schulmeyer, T. Weingärtner, A. Zabernig, Tungsten (W) Laminate Pipes for Innovative High Temperature Energy Conversion Systems, Adv. Eng. Mater. 17 (2015) 491–501. https://doi.org/10.1002/adem.201400204.

[17] C. Linsmeier, M. Rieth, J. Aktaa, T. Chikada, A. Hoffmann, J. Hoffmann, A. Houben, H. Kurishita, X. Jin, M. Li, A. Litnovsky, S. Matsuo, A. von Müller, V. Nikolic, T. Palacios, R. Pippan, D. Qu, J. Reiser, J. Riesch, T. Shikama, R. Stieglitz, T. Weber, S. Wurster, J.-H. You, Z. Zhou, Development of advanced high heat flux and plasma-facing materials, Nucl. Fusion 57 (2017) 92007, https://doi.org/10.1088/1741-4326/aa6f71.

[18] M.E. Launey, R.O. Ritchie, On the Fracture Toughness of Advanced Materials, Adv. Mater. 21 (2009) 2103–2110, https://doi.org/10.1002/adma.200803322.

[19] J.W. Coenen, Y. Mao, S. Sistla, J. Riesch, T. Hoeschen, C. Broeckmann, R. Neu, C. Linsmeier, Improved pseudo-ductile behavior of powder metallurgical tungsten short fiber-reinforced tungsten (W/W), Nucl. Mater. Energy 15 (2018) 214–219, https://doi.org/10.1016/j.nme.2018.05.001.

[20] J. Reiser, L. Garrison, H. Greuner, J. Hoffmann, T. Weingärtner, U. Jäntsch, M. Klimenkov, P. Franke, S. Bonk, C. Bonnekoh, S. Sickinger, S. Baumgärtner, D. Bolich, M. Hoffmann, R. Ziegler, J. Konrad, J. Hohe, A. Hoffmann, T. Mrotzek, M. Seiss, M. Rieth, A. Möslang, Ductilisation of tungsten (W): Tungsten laminated composites, Int. J. Refract. Met. Hard Mater. 69 (2017) 66–109, https://doi.org/10.1016/j.ijrmhm.2017.07.013.

[21] R.W. Campbell, C.D. Dickinson, Effect of melting variables on purity and properties of tungsten, in: G.M. Ault, W.F. Barclay, H.P. Munger (Eds.), High temperature materials II: Proceedings of technical conference on high temperature materials II. Conference held in Cleveland, Ohio, Apil 26-27, 1961, Interscience Publishers, New York, NY, USA, 1963, pp. 655–668.

[22] B. Gludovatz, S. Wurster, T. Weingärtner, A. Hoffmann, R. Pippan, Influence of impurities on the fracture behaviour of tungsten, Philos. Mag. 91 (2011) 3006–3020, https://doi.org/10.1080/14786435.2011.558861.

[23] M. Rieth, Tungsten for DEMO Divertors: An overview of production, basic properties, processing and divertor applications in fusion power plants. Presentation given at the Tungsten workshop, Oxford, GBR, 23 October 2013.

[24] E. Lassner, W.-D. Schubert, Tungsten: Properties, Chemistry, Technology of the Element, Alloys and Chemical Compounds, Kluwer Academic/Plenum Publishers, New York, NY, USA (1999), https://doi.org/10.1007/978-1-4615-4907-9.

[25] S. Wurster, B. Gludovatz, A. Hoffmann, R. Pippan, Fracture behaviour of tungsten–vanadium and tungsten–tantalum alloys and composites, J. Nucl. Mater. 413 (2011) 166–176, https://doi.org/10.1016/j.jnucmat.2011.04.025.

[26] T. Palacios, J.Y. Pastor, M.V. Aguirre, A. Martín, M.A. Monge, A. Muñóz, R. Pareja, Mechanical behavior of tungsten–vanadium–lanthana alloys as function of temperature, J. Nucl. Mater. 442 (2013) S277–S281, https://doi.org/10.1016/j.jnucmat.2013.02.006.

[27] M. Rieth, J. Reiser, B. Dafferner, S. Baumgärtner, The Impact of Refractory Material Properties on the Helium Cooled Divertor Design, Fusion Sci. Technol. 61 (2012) 381–384. https://doi.org/10.13182/FST12-1T3.

[28] P.L. Raffo, W.D. Klopp, W.R. Witzke, Mechanical properties of arc-melted and electron-beam-melted tungsten base alloys. NASA Technical Note NASA TN D-2561. Lewis Research Center, Cleveland, OH. National Aeronautics and Space Administration, Washington D.C., USA, 1965.

[29] C. Ren, Z.Z. Fang, M. Koopman, H. Zhang, The Effects of Molybdenum Additions on the Sintering and Mechanical Behavior of Ultrafine-Grained Tungsten, JOM 70 (2018) 2567–2573, https://doi.org/10.1007/s11837-018-3119-2.

[30] B.-S. Li, T.J. Marrow, D.E.J. Armstrong, Measuring the brittle-to-ductile transition temperature of tungsten–tantalum alloy using chevron-notched micro-cantilevers, Scr. Mater. 180 (2020) 77–82, https://doi.org/10.1016/j.scriptamat.2020.01.030.

[31] A. Argon, Strengthening Mechanisms in Crystal Plasticity, Oxford Univ. Press, Oxford, GBR, 2007. https://doi.org/10.1093/acprof:oso/9780198516002.001.0001.

[32] S.V. Nagender Naidu, P. Rama Rao (Eds.), Phase diagrams of binary tungsten alloys, 1st ed., Indian Institute of Metals, Calcutta, IND, 1991.

[33] J.J. English, Binary and ternary phase diagrams of columbium, molybdenum, tantalum, and tungsten. DMIC Report 152. Battelle Memorial Institute, Columbus, OH, USA, 1961.

[34] J.J. English, Binary and ternary phase diagrams of columbium, molybdenum, tantalum, and tungsten: Supplement to DMIC Report 152. DMIC Report 183. Battelle Memorial Institute, Columbus, OH, USA, 1963.

[35] W. Rostoker, A study of ternary phase diagrams of tungsten and tantalum. WADC Technical Report 59-492. Wright Air Development Division, Air Research and Development Command. U. S. Air Force, Wright-Patterson Air Force Base, OH, USA, 1960.

[36] I.L. Shabalin, Ultra-High Temperature Materials I, Springer, Netherlands, Dordrecht, NLD (2014), https://doi.org/10.1007/978-94-007-7587-9.

[37] R.G. Nelson, D.P. O'Keefe, A study of tungsten-technecium alloys. Technical Report CR-97099, BNWL-865. Pacific Northwest Laboratory, Richland, WA. Battelle Memorial Institute, Columbus, OH, USA, 1968.

[38] A. Luo, D.L. Jacobson, K.S. Shin, Solution softening mechanism of iridium and rhenium in tungsten at room temperature, Int. J. Refract. Met. Hard Mater. 10 (1991) 107–114, https://doi.org/10.1016/0263-4368(91)90028-M.

[39] P.L. Raffo, Yielding and fracture in tungsten and tungsten-rhenium alloys. NASA Technical Note NASA TN D-4567. Lewis Research Center, Cleveland, OH. National Aeronautics and Space Administration, Washington D.C., USA, 1968.

[40] J.R. Stephens, Dislocation structures in single-crystal tungsten and tungsten alloys, Metall. Mater. Trans. B 1 (1970) 1293–1301, https://doi.org/10.1007/BF02900246.

[41] J.L. Ratliff, D.J. Maykuth, H.R. Ogden, R.I. Jaffee, Tungsten sheet alloys with improved low-temperature ductility, Trans. Metall. Soc. AIME (1964) 490–500.

[42] W.D. Klopp, Review of ductilizing of group via elements by rhenium and other solutes. NASA Technical Note TN D-4955. Lewis Research Center, Cleveland, OH. National Aeronautics and Space Administration, Washington D.C., USA, 1968.

[43] J.L. Ratliff, D.J. Maykuth, H.R. Ogden, R.I. Jaffee, Development of a ductile tungsten sheet alloy. Research Report AD 277459. Bureau of Naval Weapons. Battelle Memorial Institute, Columbus, OH, USA, 1962.

[44] Y.-J. Hu, M.R. Fellinger, B.G. Bulter, Y. Wang, K.A. Darling, L.J. Kecskes, D.R. Trinkle, Z.-K. Liu, Solute-induced solid-solution softening and hardening in bcc tungsten, Acta Mater. 141 (2017) 304–316, https://doi.org/10.1016/j.actamat.2017.09.019.

[45] W.D. Klopp, P.L. Raffo, W.R. Witzke, Mechanical properties of dilute tungsten-rhenium alloys prepared by electron beam and arc melting. NASA Technical Note NASA TN D-3483. Lewis Research Center, Cleveland, OH. National Aeronautics and Space Administration, Washington D.C., USA, 1966.

[46] W.D. Klopp, P.L. Raffo, W.R. Witzke, Ductility and strength of dilute tungsten-rhenium alloys. NASA Technical Memorandum NASA TM-X-52134. Lewis Research Center. National Aeronautics and Space Administration, Washington D. C., USA, 1965.

[47] H. Sicius, Mangangruppe: Elemente der siebten Nebengruppe, in: H. Sicius (Ed.), Handbuch der chemischen Elemente. (textbook in german language), Springer, Berlin, DEU, 2020, pp. 1–40. https://doi.org/10.1007/978-3-662-55944-4_12-2.

[48] C. Ren, Z.Z. Fang, M. Koopman, B. Butler, J. Paramore, S. Middlemas, Methods for improving ductility of tungsten - A review, Int. J. Refract. Met. Hard Mater. 75 (2018) 170–183, https://doi.org/10.1016/j.ijrmhm.2018.04.012.

[49] G.A. Geach, J.E. Hughes, The alloys of rhenium with molybdenum or with tungsten and having good high temperature properties, in: F. Benesovsky (Ed.), Warmfeste und korrosionsbeständige Sinterwerkstoffe: Vorträge, gehalten auf dem 2. Plansee Seminar; 19. bis 23. Juni 1955, Reutte Tirol, Metallwerk Plansee, Reutte, AUT, 1956, pp. 245–253.

[50] B. Gludovatz, S. Wurster, A. Hoffmann, R. Pippan, Fracture toughness of polycrystalline tungsten alloys, Int. J. Refract. Met. Hard Mater. 28 (2010) 674–678, https://doi.org/10.1016/j.ijrmhm.2010.04.007.

[51] R. Eck, H. Bildstein, F. Simader, R. Stickler, J. Tinzl, Behaviour of tungsten, molybdenum, and alloys under unusual heating conditions, in: H. Bildstein, H.M. Ortner (Eds.), 12th International Plansee Seminar '89: Proceedings: High Temperature and Wear Resistant Materials in a World of Changing Technology. May 8th to 12th, 1989, Reutte, Tirol, Austria, Metallwerk Plansee, Reutte, AUT, 1989, pp. 793–805.

[52] A. Hasegawa, M. Fukuda, K. Yabuuchi, S. Nogami, Neutron irradiation effects on the microstructural development of tungsten and tungsten alloys, J. Nucl. Mater. 471 (2016) 175–183, https://doi.org/10.1016/j.jnucmat.2015.10.047.

[53] S.J. Zinkle, Fusion materials science: Overview of challenges and recent progress, Phys. Plasmas 12 (2005) 58101, https://doi.org/10.1063/1.1880013.

[54] S.J. Zinkle, L.L. Snead, Designing Radiation Resistance in Materials for Fusion Energy, Annu. Rev. Mater. Res. 44 (2014) 241–267, https://doi.org/10.1146/annurev-matsci-070813-113627.

[55] M. Rieth, R. Doerner, A. Hasegawa, Y. Ueda, M. Wirtz, Behavior of tungsten under irradiation and plasma interaction, J. Nucl. Mater. 519 (2019) 334–368, https://doi.org/10.1016/j.jnucmat.2019.03.035.

[56] M. Fukuda, N.A.P. Kiran Kumar, T. Koyanagi, L.M. Garrison, L.L. Snead, Y. Katoh, A. Hasegawa, Neutron energy spectrum influence on irradiation hardening and microstructural development of tungsten, J. Nucl. Mater. 479 (2016) 249–254, https://doi.org/10.1016/j.jnucmat.2016.06.051.

[57] L.M. Garrison, Y. Katoh, N.A.P.K. Kumar, Mechanical properties of single-crystal tungsten irradiated in a mixed spectrum fission reactor, J. Nucl. Mater. 518 (2019) 208–225, https://doi.org/10.1016/j.jnucmat.2019.02.050.

[58] D. Terentyev, M. Vilémová, C. Yin, J. Veverka, A. Dubinko, J. Matějíček, Assessment of mechanical properties of SPS-produced tungsten including effect of neutron irradiation, Int. J. Refract. Met. Hard Mater. 89 (2020) 105207, , https://doi.org/10.1016/j.ijrmhm.2020.105207.

[59] R.G. Abernethy, J.S.K.-L. Gibson, A. Giannattasio, J.D. Murphy, O. Wouters, S. Bradnam, L.W. Packer, M.R. Gilbert, M. Klimenkov, M. Rieth, H.-C. Schneider, C.D. Hardie, S.G. Roberts, D.E.J. Armstrong, Effects of neutron irradiation on the brittle to ductile transition in single crystal tungsten, J. Nucl. Mater. 527 (2019) 151799, , https://doi.org/10.1016/j.jnucmat.2019.151799.

[60] R.K. Williams, F.W. Wiffen, J. Bentley, J.O. Stiegler, Irradiation induced

precipitation in tungsten based, W–Re alloys, Metall. Trans. 14 (1983) 655–666, https://doi.org/10.1007/BF02643781.

[61] P. Krautwasser, H. Derz, E. Kny, Influence of fast neutron fluence on the DBTT of W, W10Re, and W3.4Ni1.6Fe, in: H. Bildstein, H.M. Ortner (Eds.), 12th International Plansee Seminar '89: Proceedings: High Temperature and Wear Resistant Materials in a World of Changing Technology. May 8th to 12th, 1989, Reutte, Tirol, Austria, Metallwerk Plansee, Reutte, AUT, 1989, pp. 673–681.

[62] A. Hasegawa, M. Fukuda, S. Nogami, K. Yabuuchi, Neutron irradiation effects on tungsten materials, Fusion Eng. Des. 89 (2014) 1568–1572, https://doi.org/10.1016/j.fusengdes.2014.04.035.

[63] M. Fukuda, S. Nogami, A. Hasegawa, H. Usami, K. Yabuuchi, T. Muroga, Tensile properties of K-doped W–3%Re, Fusion Eng. Des. 89 (2014) 1033–1036, https://doi.org/10.1016/j.fusengdes.2014.02.062.

[64] H. Bolt, V. Barabash, W. Krauss, J. Linke, R. Neu, S. Suzuki, N. Yoshida, ASDEX Upgrade Team, Materials for the plasma-facing components of fusion reactors, J. Nucl. Mater. 329–333 (2004) 66–73, https://doi.org/10.1016/j.jnucmat.2004.04.005.

[65] S. Watanabe, S. Nogami, J. Reiser, M. Rieth, S. Sickinger, S. Baumgärtner, T. Miyazawa, A. Hasegawa, Tensile and impact properties of tungsten-rhenium alloy for plasma-facing components in fusion reactor, Fusion Eng. Des. 148 (2019) 111323, , https://doi.org/10.1016/j.fusengdes.2019.111323.

[66] S. Nogami, A. Hasegawa, M. Fukuda, S. Watanabe, J. Reiser, M. Rieth, Tungsten modified by potassium doping and rhenium addition for fusion reactor applications, Fusion Eng. Des. 152 (2020) 111445, , https://doi.org/10.1016/j.fusengdes.2019.111445.

[67] A.A.N. Németh, J. Reiser, D.E.J. Armstrong, M. Rieth, The nature of the brittle-to-ductile transition of ultra fine grained tungsten (W) foil, Int. J. Refract. Met. Hard Mater. 50 (2015) 9–15, https://doi.org/10.1016/j.ijrmhm.2014.11.005.

[68] V. Nikolić, S. Wurster, D. Firneis, R. Pippan, Improved fracture behavior and microstructural characterization of thin tungsten foils, Nucl. Mater. Energy 9 (2016) 181–188, https://doi.org/10.1016/j.nme.2016.06.003.

[69] V. Nikolić, S. Wurster, D. Firneis, R. Pippan, Fracture toughness evaluation of UFG tungsten foil, Int. J. Refract. Met. Hard Mater. 76 (2018) 214–225, https://doi.org/10.1016/j.ijrmhm.2018.06.008.

[70] P. Lied, W. Pantleon, C. Bonnekoh, S. Bonk, A. Hoffmann, J. Reiser, M. Rieth, Comparison of K-doped and pure cold-rolled tungsten sheets: Tensile properties and ductile-to-brittle-transition. (manuscript under review).

[71] C. Bonnekoh, U. Jäntsch, J. Hoffmann, H. Leiste, A. Hartmaier, D. Weygand, A. Hoffmann, J. Reiser, The brittle-to-ductile transition in cold rolled tungsten plates: Impact of crystallographic texture, grain size and dislocation density on the transition temperature, Int. J. Refract. Met. Hard Mater. 78 (2019) 146–163, https://doi.org/10.1016/j.ijrmhm.2018.09.010.

[72] V.I. Trefilov, Y.V. Milman, Physical basis of thermomechanical treatment of refractory metals, in: H. Bildstein, H.M. Ortner (Eds.), 12th International Plansee Seminar '89: Proceedings: High Temperature and Wear Resistant Materials in a World of Changing Technology. May 8th to 12th, 1989, Reutte, Tirol, Austria, Metallwerk Plansee, Reutte, AUT, 1989, pp. 107–131.

[73] Deutsche Institut für Normung e.V. DIN, Geometrical Product Specifications (GPS) – Surface texture: Profile method: Terms, definitions and surface texture parameters, Beuth, Berlin, DEU, 2010.

[74] ASTM International, ASTM E399-19, Test Method for Linear-Elastic Plane-Strain Fracture Toughness KIc of Metallic Materials, 19th ed., ASTM International, West Conshohocken, PA, USA, 2019.

[75] T. Palacios, J.Y. Pastor, Influence of the notch root radius on the fracture toughness of brittle metals: Nanostructure tungsten alloy, a case study, Int. J. Refract. Met. Hard Mater. 52 (2015) 44–49, https://doi.org/10.1016/j.ijrmhm.2015.05.012.

[76] B.S. Kong, J.H. Shin, C. Jang, H.C. Kim, Measurement of Fracture Toughness of Pure Tungsten Using a Small-Sized Compact Tension Specimen, Materials 13 (2020) 244, https://doi.org/10.3390/ma13010244.

[77] T.L. Anderson, Fracture Mechanics: Fundamentals and Applications, Fourth Edition, CRC Press, Boca Raton, FL, USA, 2017, , https://doi.org/10.1201/9781315370293.

[78] ASTM International, ASTM E1558-09, Electrolytic Polishing of Metallographic Specimens, 9th ed., ASTM International, West Conshohocken, PA, USA, 2014.

[79] N. Hansen, C.Y. Barlow, Plastic deformation of metals and alloys, in: D.E. Laughlin, K. Hōno (Eds.), Physical metallurgy, fifth ed., Elsevier, Amsterdam, NLD, 2014, pp. 1681–1764. https://doi.org/10.1016/B978-0-444-53770-6.00017-4.

[80] S. Zaefferer, New developments of computer-aided crystallographic analysis in transmission electron microscopy, J. Appl. Crystallogr. 33 (2000) 10–25, https://doi.org/10.1107/S0021889899010894.

[81] K.-H. Schwalbe, B. Neale, A procedure for determining the fracture behaviour of materials: The unified fracture mechanics test method EFAM GTP 94, Fat Frac Eng Mat Struct 18 (1995) 413–424, https://doi.org/10.1111/j.1460-2695.1995.tb01185.x.

[82] Q. Wei, L.J. Kecskes, Effect of low-temperature rolling on the tensile behavior of commercially pure tungsten, Mater. Sci. Eng., A 491 (2008) 62–69, https://doi.org/10.1016/j.msea.2008.01.013.

[83] R. Hielscher, C.B. Silbermann, E. Schmidl, J. Ihlemann, Denoising of crystal orientation maps, J. Appl. Crystallogr. 52 (2019) 984–996, https://doi.org/10.1107/S1600576719009075.

[84] I. Brough, P.S. Bate, F.J. Humphreys, Optimising the angular resolution of EBSD, Mater. Sci. Technol. 22 (2006) 1279–1286, https://doi.org/10.1179/174328406X130902.

[85] F.J. Humphreys, Review Grain and subgrain characterisation by electron backscatter diffraction, J. Mater. Sci. 36 (2001) 3833–3854, https://doi.org/10.1023/

A:1017973432592.

[86] D.G. Brandon, The structure of high-angle grain boundaries, Acta Metall. 14 (1966) 1479–1484, https://doi.org/10.1016/0001-6160(66)90168-4.

[87] O. Engler, V. Randle, Introduction to texture analysis: Macrotexture, microtexture, and orientation mapping, second. ed., CRC Press, Boca Raton, FL, USA, 2010.

[88] U.F. Kocks, The representation of orientatoins and textures, in: U.F. Kocks, C.N. Tomé, H.-R. Wenk (Eds.), Texture and anisotropy: Preferred orientations in polycrystals and their effect on materials properties, first ed., Cambridge Univ. Press, Cambridge, GBR, 2000, 44-101.

[89] S.I. Wright, M.M. Nowell, D.P. Field, A review of strain analysis using electron backscatter diffraction, Microsc. Microanal. 17 (2011) 316–329, https://doi.org/10.1017/S1431927611000055.

[90] B. Horváth, R. Schäublin, Y. Dai, Flash electropolishing of TEM lamellas of irradiated tungsten, Nuclear Inst, and Methods in Physics Research B 449, 2019, pp. 29–34, , https://doi.org/10.1016/j.nimb.2019.04.047.

[91] T. Koyanagi, N.A.P.K. Kumar, T. Hwang, L.M. Garrison, X. Hu, L.L. Snead, Y. Katoh, Microstructural evolution of pure tungsten neutron irradiated with a mixed energy spectrum, J. Nucl. Mater. 490 (2017) 66–74, https://doi.org/10.1016/j.jnucmat.2017.04.010.

[92] H. Kurishita, A. Oishi, H. Kubo, H. Yoshinaga, Grain boundary fracture in molybdenum bicrystals with various ⟨110⟩ symmetric tilt boundaries, Trans. JIM 26 (1985) 341–352, https://doi.org/10.2320/matertrans1960.26.341.

[93] I.M. Mikhailovskij, T.I. Mazilova, V.N. Voyevodin, A.A. Mazilov, Inherent strength of grain boundaries in tungsten, Phys. Rev. B 83 (2011) 757, https://doi.org/10.1103/PhysRevB.83.134115.

[94] L. Tanure, D. Terentyev, J. Riesch, K. Verbeken, Evolution of microstructure, texture and grain boundary character distribution of potassium doped tungsten fibers annealed at variable temperatures, J. Phys.: Conf. Ser. 1270 (2019) 12038. https://doi.org/10.1088/1742-6596/1270/1/012038.

[95] D. Terentyev, W. van Renterghem, L. Tanure, A. Dubinko, J. Riesch, S. Lebediev, T. Khvan, K. Verbeken, J.W. Coenen, E.E. Zhurkin, Correlation of microstructural and mechanical properties of K-doped tungsten fibers used as reinforcement of tungsten matrix for high temperature applications, Int. J. Refract. Met. Hard Mater. 79 (2019) 204–216, https://doi.org/10.1016/j.ijrmhm.2018.12.007.

[96] S. Kobayashi, S. Tsurekawa, T. Watanabe, Evolution of grain boundary microstructures in molybdenum by thermomechanical processing from single crystals, in: A.D. Rollett (Ed.), Applications of Texture Analysis, John Wiley & Sons, Hoboken, NJ, USA, 2008, pp. 681–692.

[97] L. Priester, Grain boundaries: From theory to engineering, Springer, Dordrecht, NLD (2013), https://doi.org/10.1007/978-94-007-4969-6.

[98] N.K. Sharma, S. Shekhar, Cut-off deviation for CSL boundaries in recrystallized face-centered cubic materials, Philos. Mag. 97 (2017) 2004–2017, https://doi.org/10.1080/14786435.2017.1322730.

[99] C.R. Weinberger, B.L. Boyce, C.C. Battaile, Slip planes in bcc transition metals, Int. Mater. Rev. 58 (2013) 296–314, https://doi.org/10.1179/1743280412Y.0000000015.

[100] O. El-Atwani, W.S. Cunningham, E. Esquivel, M. Li, J.R. Trelewicz, B.P. Uberuaga, S.A. Maloy, In-situ irradiation tolerance investigation of high strength ultrafine tungsten-titanium carbide alloy, Acta Mater. 164 (2019) 547–559, https://doi.org/10.1016/j.actamat.2018.10.038.

[101] D. Caillard, Geometry and kinetics of glide of screw dislocations in tungsten between 95K and 573K, Acta Mater. 161 (2018) 21–34, https://doi.org/10.1016/j.actamat.2018.09.009.

[102] L.P. Kubin, Dislocations, Mesoscale Simulations and Plastic Flow, first ed., Oxford Univ. Press, Oxford, GBR, 2013. https://doi.org/10.1093/acprof:oso/9780198525011.001.0001.

[103] D. Brunner, Comparison of flow-stress measurements on high-purity tungsten single crystals with the kink-pair theory, Mater. Trans., JIM 41 (2000) 152–160, https://doi.org/10.2320/matertrans1989.41.152.

[104] D. Caillard, J.-L. Martin, Thermally activated mechanisms in crystal plasticity, Pergamon, Oxford, GBR, 2003.

[105] J.R. Stephens, Review of the deformation behavior of tungsten at temperatures less than 0.2 absolute melting temperature. NASA Technical Memorandum NASA TM X-2482. Lewis Research Center, Cleveland, OH. National Aeronautics and Space Administration, Washington D.C., USA, 1972.

[106] J. Reiser, M. Rieth, B. Dafferner, A. Hoffmann, Charpy impact properties of pure tungsten plate material in as-received and recrystallized condition, J. Nucl. Mater. 442 (2013) S204–S207, https://doi.org/10.1016/j.jnucmat.2012.10.037.

[107] M.J. Pfeifenberger, V. Nikolić, S. Žák, A. Hohenwarter, R. Pippan, Evaluation of the intergranular crack growth resistance of ultrafine grained tungsten materials, Acta Mater. 176 (2019) 330–340, https://doi.org/10.1016/j.actamat.2019.06.051.

[108] J. Reiser, A. Hartmaier, Elucidating the dual role of grain boundaries as dislocation sources and obstacles and its impact on toughness and brittle-to-ductile transition, Sci. Rep. 10 (2020) 2739, https://doi.org/10.1038/s41598-020-59405-5.

[109] C. Bonnekoh, P. Lied, W. Pantleon, T. Karcher, H. Leiste, A. Hoffmann, J. Reiser, M. Rieth, The brittle-to-ductile transition in cold-rolled tungsten sheets (accepted: DOI: https://doi.org/10.1016/j.ijrmhm.2020.105347 manuscript): On the loss of room-temperature ductility after annealing and the phenomenon of 45° embrittlement. doi: 10.1016/j.ijrmhm.2020.105347.

[110] X. Sauvage, G. Wilde, S.V. Divinski, Z. Horita, R.Z. Valiev, Grain boundaries in ultrafine grained materials processed by severe plastic deformation and related phenomena, Mater. Sci. Eng., A 540 (2012) 1–12, https://doi.org/10.1016/j.msea.2012.01.080.

[111] G. Wilde, Physical Metallurgy of Nanocrystalline Metals, in: D.E. Laughlin, K. Hōno (Eds.), Physical metallurgy, fifth ed., Elsevier, Amsterdam, NLD, 2014, pp.

2707–2805. https://doi.org/10.1016/B978-0-444-53770-6.00026-5.

[112] E. Bitzek, P. Gumbsch, Mechanisms of dislocation multiplication at crack tips, Acta Mater. 61 (2013) 1394–1403, https://doi.org/10.1016/j.actamat.2012.11.016.

[113] V.V. Bulatov, L.L. Hsiung, M. Tang, A. Arsenlis, M.C. Bartelt, W. Cai, J.N. Florando, M. Hiratani, M. Rhee, G. Hommes, T.G. Pierce, T.D. de La Rubia, Dislocation multi-junctions and strain hardening, Nature 440 (2006) 1174–1178, https://doi.org/10.1038/nature04658.

[114] S. Krimpalis, K. Mergia, S. Messoloras, A. Dubinko, D. Terentyev, K. Triantou, J. Reiser, G. Pintsuk, Comparative study of the mechanical properties of different tungsten materials for fusion applications, Phys. Scr. T170 (2017) 14068, https://doi.org/10.1088/1402-4896/aa9292.

[115] C. Ren, Z.Z. Fang, L. Xu, J.P. Ligda, J.D. Paramore, B.G. Butler, An investigation of the microstructure and ductility of annealed cold-rolled tungsten, Acta Mater. 162 (2019) 202–213, https://doi.org/10.1016/j.actamat.2018.10.002.

[116] Z. Chen, W. Han, J. Yu, L. Kecskes, K. Zhu, Q. Wei, Microstructure and helium irradiation performance of high purity tungsten processed by cold rolling, J. Nucl. Mater. 479 (2016) 418–425, https://doi.org/10.1016/j.jnucmat.2016.07.038.

[117] Y. Oh, N. Kwak, K. Lee, W.-S. Ko, H.N. Han, Ductility enhancement of tungsten after plastic deformation, J. Alloys Compd. 787 (2019) 801–814, https://doi.org/10.1016/j.jallcom.2019.02.097.

[118] L.E. Murr, Dislocation Ledge Source: Dispelling the Myth of Frank-Read Source Importance, Metall. Mater. Trans. A 47 (2016) 5811–5826, https://doi.org/10.1007/s11661-015-3286-5.

[119] I. Issa, A. Hohenwarter, R. Fritz, D. Kiener, Fracture properties of ultrafine grain chromium correlated to single dislocation processes at room temperature, J. Mater. Res. 34 (2019) 2370–2383, https://doi.org/10.1557/jmr.2019.140.

[120] M. Tanaka, K. Higashida, T. Shimokawa, T. Morikawa, Brittle-Ductile Transition in Low Carbon Steel Deformed by the Accumulative Roll Bonding Process, Mater. Trans., JIM 50 (2009) 56–63, https://doi.org/10.2320/matertrans.MD200817.

[121] W.D. Klopp, P.L. Raffo, Effect of purity and structure on recrystallization, grain growth, ductility, tensile, and creep properties of arc-melted tunsten. NASA Technical Note TN D-2503. Lewis Research Center, Cleveland, OH. National Aeronautics and Space Administration, Washington D.C., USA, 1964.

[122] J. Riedle, Bruchwiderstand in Wolfram-Einkristallen: Einfluß der kristallographischen Orientierung, der Temperatur und der Lastrate: (PhD-thesis in german language). VDI-Verl., Stuttgart, DEU, 1995.

[123] M. Zhang, S. Yang, F. Wan, Competition mechanism of brittle–ductile transition of metals under tensile condition, Mechanics of Materials 137 (2019) 103138, , https://doi.org/10.1016/j.mechmat.2019.103138.

[124] D. Rupp, S.M. Weygand, Experimental investigation of the fracture toughness of polycrystalline tungsten in the brittle and semi-brittle regime, J. Nucl. Mater. 386–388 (2009) 591–593, https://doi.org/10.1016/j.jnucmat.2008.12.184.

[125] J. Reiser, J. Hoffmann, U. Jäntsch, M. Klimenkov, S. Bonk, C. Bonnekoh, A. Hoffmann, T. Mrotzek, M. Rieth, Ductilisation of tungsten (W): On the increase of strength AND room-temperature tensile ductility through cold-rolling, Int. J. Refract. Met. Hard Mater. 64 (2017) 261–278, https://doi.org/10.1016/j.ijrmhm.2016.10.018.

[126] C. Marichal, H. van Swygenhoven, S. van Petegem, C. Borca, 110 Slip with 112 slip traces in bcc Tungsten, Sci. Rep. 3 (2013) 2547, https://doi.org/10.1038/srep02547.

[127] R. Gröger, A.G. Bailey, V. Vitek, Multiscale modeling of plastic deformation of molybdenum and tungsten: I. Atomistic studies of the core structure and glide of

1/2⟨111⟩ screw dislocations at 0 K, Acta Mater. 56 (2008) 5401–5411, https://doi.org/10.1016/j.actamat.2008.07.018.

[128] K. Srivastava, R. Gröger, D. Weygand, P. Gumbsch, Dislocation motion in tungsten: Atomistic input to discrete dislocation simulations, Int. J. Plast. 47 (2013) 126–142, https://doi.org/10.1016/j.ijplas.2013.01.014.

[129] P.B. Hirsch, S.G. Roberts, J. Samuels, The Brittle-Ductile Transition in Silicon. II. Interpretation, Proc. R. Soc. London, Ser. A 421 (1989) 25–53. https://doi.org/10.1098/rspa.1989.0002.

[130] S.G. Roberts, Modelling the Brittle to Ductile Transition in Single Crystals, in: H.O. Kirchner, L.P. Kubin, V. Pontikis (Eds.), Computer Simulation in Materials Science, Springer, Dordrecht, NLD, 1996, pp. 409–433, , https://doi.org/10.1007/978-94-009-1628-9_22.

[131] A. Hartmaier, P. Gumbsch, The brittle-to-ductile transition and dislocation activity at crack tips, J. Comput.-Aided Mater. Des. 6 (1999) 145–155, https://doi.org/10.1023/A:1008706022897.

[132] A. Hartmaier, Modeling of Crack-Tip Plasticity in Tungsten Single Crystals, PhD-thesis DEU, Stuttgart, 2000.

[133] A. Hartmaier, P. Gumbsch, Scaling relations for crack-tip plasticity, Philos. Mag. A 82 (2002) 3187–3200, https://doi.org/10.1080/01418610208240432.

[134] N. Kamikawa, X. Huang, N. Tsuji, N. Hansen, Strengthening mechanisms in nanostructured high-purity aluminium deformed to high strain and annealed, Acta Mater. 57 (2009) 4198–4208, https://doi.org/10.1016/j.actamat.2009.05.017.

[135] O. El-Atwani, J.A. Hinks, G. Greaves, S. Gonderman, T. Qiu, M. Efe, J.P. Allain, In-situ TEM observation of the response of ultrafine- and nanocrystalline-grained tungsten to extreme irradiation environments, Sci. Rep. 4 (2014) 4716, https://doi.org/10.1038/srep04716.

[136] D.E.J. Armstrong, T.B. Britton, Effect of dislocation density on improved radiation hardening resistance of nano-structured tungsten–rhenium, Mater. Sci. Eng., A 611 (2014) 388–393, https://doi.org/10.1016/j.msea.2014.06.013.

[137] M. Fukuda, A. Hasegawa, T. Tanno, S. Nogami, H. Kurishita, Property change of advanced tungsten alloys due to neutron irradiation, J. Nucl. Mater. 442 (2013) S273–S276, https://doi.org/10.1016/j.jnucmat.2013.03.058.

[138] Z.X. Zhang, D.S. Chen, W.T. Han, A. Kimura, Irradiation hardening in pure tungsten before and after recrystallization, Fusion Eng. Des. 98–99 (2015) 2103–2107, https://doi.org/10.1016/j.fusengdes.2015.06.192.

[139] G.D. Samolyuk, Y.N. Osetsky, R.E. Stoller, The influence of transition metal solutes on the dislocation core structure and values of the Peierls stress and barrier in tungsten, issn 0953-8984, J. Phys.: Condensed Matter 25 (2) (2013) 025403, https://doi.org/10.1088/0953-8984/25/2/025403.

[140] Y. Zhao, J. Marian, Direct prediction of the solute softening-to-hardening transition in W-Re alloys using stochastic simulations of screw dislocation motion, Modelling Simul. Mater. Sci. Eng. 26 (2018) 45002, https://doi.org/10.1088/1361-651X/aaaecf.

[141] J.R. Stephens, W.R. Witzke, Alloy softening in group via metals alloyed with rhenium. NASA Technical Note NASA TN D-7000. Lewis Research Center, Cleveland, OH. National Aeronautics and Space Administration, Washington D.C., USA, 1970.

[142] T. Tsuru, M. Wakeda, T. Suzudo, M. Itakura, S. Ogata, Anomalous solution softening by unique energy balance mediated by kink mechanism in tungsten-rhenium alloys, J. Theor. Appl. Phys. 127 (2020) 25101, https://doi.org/10.1063/1.5131279.